Catalysis Science & Technology

Accepted Manuscript

This article can be cited before page numbers have been issued, to do this please use: V. Marakatti, M. Ronda-Lloret, M. Krajci, B. Joseph, C. Marini, J. J. Delgado, F. Devred, R. N. Shiju and E. M. Gaigneaux, *Catal. Sci. Technol.*, 2022, DOI: 10.1039/D1CY01956B.

ROYAL SOCIETY OF CHEMISTRY

rsc.li/catalysis

View Article Online
DOI: 10.1039/D1CY01956B

Highly Active and Stable Co (Co_3O_4)_Sm_2O_3 Nano-crystallites Derived from Sm_2Co_7 and $SmCo_5$ Intermetallic Compounds in NH_3 Synthesis and CO_2 Conversion

Vijaykumar S Marakatti,[a*] Maria Ronda-Lloret,[b] M. Krajčí,[c] Boby Joseph,[d] Carlo Marini,[e] Juan Jose Delgado,[f] François Devred, [a] N. Raveendran Shiju,[b] Eric M Gaigneaux[a*]

[a]*Institute of Condensed Matter and Nanosciences (IMCN), Molecular chemistry, Solids and caTalysis (MOST), Université catholique de Louvain (UCLouvain), Place Louis Pasteur, B-1348 Louvain-la-Neuve, Belgium.*

[b] *Van't Hoff Institute for Molecular Sciences, University of Amsterdam, Science Park 904, Amsterdam 1090 GD, The Netherlands.*

[c] *Institute of Physics, Slovak Academy of Sciences, Bratislava SK-84511, Slovakia*

[d]*Elettra-Sincrotrone Trieste S. C. p. A., S.S. 14, Km 163.5 in Area Science Park, Basovizza 34149, Italy*

[e]*ALBA Synchrotron Light Source, Carrer de la Llum 2-26, Cerdanyola del Vallès, Barcelona, Spain*

[f]*Departamento de Ciencia de los Materiales e Ingeniería Metalúrgica y Química Inorgánica, e IMEYMAT, Instituto Universitario de Investigación en Microscopía Electrónica y Materiales, Universidad de Cádiz, Puerto Real 11510, Spain*

*Corresponding author: eric.gaigneaux@uclouvain.be, chmvijay@gmail.com

Phone: +32 (0)10 47 36 65 - Fax: +32 (0)10 47 36 49

View Article Online
DOI: 10.1039/D1CY01956B

Abstract

Intermetallic compounds (IMCs) are interesting materials in the field of heterogeneous catalysis due to their ordered structure and tunable electronic properties. These IMCs can act as precursor to synthesize metal/metal oxide composite catalysts that are more active than just the starting IMCs. In this work, Sm_2Co_7 and $SmCo_5$ IMCs were used as precursors to prepare highly active and stable Co_SmO, Co_Sm_2O_3 and Co_3O_4_Sm_2O_3 catalysts via controlled modification. Transmission electron microscopy (TEM) demonstrated that Co and Sm_2O_3 Nano crystallites were formed after the modification of the starting IMC. IMCs derived Co_SmO and Co_Sm_2O_3 were stable and active in NH_3 synthesis with very low activation energy of 55 and 77 kJ/mol respectively. The structural, morphological and surface characterization revealed that a strong metal support interaction existed between Co and Sm_2O_3 (electronic effect) along with the presence of surface steps and edges of Co nano crystallites (structural effect) that activated the N_2 at low temperature (360 °C). Similarly, Co_3O_4_Sm_2O_3 derived from the IMC were found to exhibit high CO_2 and butane conversion in butane dry reforming at low temperature (550 ˚C) with excellent stability. The study revealed that the presence of Co_3O_4 and Sm_2O_3 active sites in close proximity (geometrical effect) promoted the simultaneous adsorption or activation of butane and CO_2. The Co_Sm_2O_3 and Co_3O_4_Sm_2O_3 derived from IMCs exhibited superior catalytic performance in both NH_3 synthesis and butane dry reforming compared to similar compositional catalyst synthesized by hydrothermal route. These studies pave the way to potential uses of IMCs as precursors to derive composite metal/metal oxide catalysts that are highly stable and active despite their low surface areas.

Keywords: Intermetallic; Ammonia synthesis; Reforming; Nano catalyst; Carbon dioxide

View Article Online
DOI: 10.1039/D1CY01956B

1.Introduction

Intermetallic compounds (IMCs) are ordered structures with fixed atomic positions formed by combining two or more metals.[1, 2] IMCs display exceptional structural properties accompanied by changes in the electronic properties.[3, 4] These geometrically and electronically tuned compounds are outstanding catalysts compared to their monometallic and alloy counterparts in several chemical reactions.[5-8] Due to their ordered structures and occasionally to their instability in reaction environments, IMCs are found to be potential precursor for the synthesis of different composite catalysts in various catalytic processes.[9] Pd-GaO_x/Al_2O_3 derived from the Pd_5Ga_3 IMC was highly active in methane combustion reaction.[10] PdZn/ZnO derived from PdZn IMC was an excellent catalyst in methanol steam reforming (MSR) reaction.[11] Pt−MnO_x/CeO_2 obtained from PtMn IMC allowed complete conversion at 180 °C in toluene combustion reaction.[12] $Ce_{50}Ni_{45}Au_5$ IMC derived Ni-Au/CeO_2 exhibited superior activity in CO oxidation.[13] Ni/ThO_2 obtained by decomposition of $ThNi_5$ IMC was highly active compared to Ni/ThO_2 prepared by wet impregnating method in hydrocarbon synthesis.[14]

Due to the ordered structure and strong covalent bond between the metals in IMCs, creation of novel active sites occurs from the destruction/instability of IM structure, and were found to be highly active in a certain reaction. As it is not easy to construct such active sites by bottom-up synthesis methods, using IMCs is a good option due to their unique crystal structure, strong metal-metal bond (ligand effect) and fixed atomic positions in the structure. These properties of IMCs increase the probability of interaction between the post modified metal-metal oxide or metal oxide-metal oxide catalyst. Under such situation, the structural and electronic properties IMCs act as excellent precursors for the synthesis of these active sites. For example, NiGe IMC forms a highly active γ-NiOOH phase during oxygen evolution reaction, but synthesis of such active γ-NiOOH species by other method is a difficult task.[15]

Under such circumstances applying IMCs as catalyst precursors will benefit in generating such highly active sites that catalyse reactions in more superior way. These active sites can be created *in situ* under reaction conditions or can be formed *ex situ* via appropriate modification.[12, 13]

In 1976, it was reported that rare earth IMCs completely decompose to metal nitride and metal under NH_3 synthesis and the metallic interfaces are the real active sites in the reaction.[16] But, limited characterization of the catalyst (only XRD was reported) could not provide much insights on the exact active site and surface catalytic properties. Contrary to this, $LaNi_5$ IMC was reported for NH_3 synthesis recently.[17] The detailed characterization showed that Ni/LaN is formed on the surface of $LaNi_5$, keeping intact the IM structure. This surface Ni activates the H_2 , whereas LaN activate the N_2 in the reaction. This uncertainty about the nature of the active sites inhibits for an in-depth understanding of the catalytic properties. Here we report a systematic investigation of $SmCo_5$ and Sm_2Co_7 IMCs derived catalysts for the activation of N_2 and CO_2 using a number of microscopic characterization techniques.

The activation of inert molecules such as CO_2 and N_2 requires high energy due to their linear symmetric structure and strong bond. Activation of N_2 is a significant step in ammonia (NH_3) synthesis. Today, a typical commercial plant for the NH_3 synthesis uses a high-energy consuming iron oxide catalyst (Temperature = 500–600°C and pressure = 20–40 MPa), which is similar as it was formulated 100 years before, with very minute improvements.[18] The drastic conditions required by such Fe based catalyst, stipulates to look for alternative catalysts. In this regard, Ruthenium (Ru) based catalysts has emerged as second-generation catalysts. But their high cost and tendency to H_2 poisoning at high pressure hinder their industrial application. Alternatively to Ru, Cobalt (Co) based catalysts remained as a potential catalyst for N_2 activation, provided an appropriate support and promoter.[18] Several Co catalysts promoted by K_2O, Cs_2O, BaO and La_2O_3 were reported for the NH_3 synthesis.[19-23] However, those

still require relatively high temperature and pressure conditions with very high activation energy (90-110 k J/mol). Recently, Co/LiH or BaH_2, $Co/12CaO.7Al_2O_3$ exhibited high activity at milder reaction conditions with low activation energies (52-58 kJ/mol) but are difficult to handle and synthesize at large scale.[24-26] Herein, we report the nanocrystalline $Co\_Sm_2O_3$ derived from Sm_2Co_7 and $SmCo_5$ IMCs as an active and highly stable catalyst for the activation of N_2 in NH_3 synthesis.

The greenhouse effect caused by the remarkable increase of CO_2 emissions into the atmosphere is an essential and urgent problem to be solved. We should convert CO_2 to value-added chemicals.[27] In this direction, methane dry reforming (CO_2+CH_4) to syngas (CO+H_2) is an outstanding process to obtain high value-added chemicals.[28] However, this reaction demands high energy (700-900°C) and catalysts deactivate within few hours due to surface coke deposition or sintering of the active sites. Butane is thermodynamically less stable ($\Delta G°_{(n*C4-H10)}$ = -16.6 kJ/mol) than CH_4 ($\Delta G°_{(CH4)}$ = -50.5 kJ/mol).[29] Thus, we are interested in butane dry reforming, as the reaction temperature can be lowered.[30] However, the formation of coke through the Boudouard reaction ($2CO \rightarrow CO_2$+C) and cracking of butane still take place. Active catalysts are Co and Ni supported on Al_2O_3, SiO_2 or TiO_2.[31] $Co_3O_4\_Sm_2O_3$ catalysts derived from Sm_2Co_7 and $SmCo_5$ IMCs are promising materials for the butane dry reforming reaction.

Herein following a different approach, we use the Sm_2Co_7 and $SmCo_5$ IMC as catalyst precursors. Heating Sm_2Co_7 and $SmCo_5$ IMCs under different gases resulted in diverse composite catalysts (Co_SmO, $Co\_Sm_2O_3$ and $Co_3O_4\_Sm_2O_3$), which are active in NH_3 synthesis and CO_2 conversion. Catalysts with similar composition but synthesized by the hydrothermal route were compared with the IMC-derived catalysts in both the reactions. The reaction mechanism over these two different types of catalysts were inferred by kinetics of reaction and DFT calculations. The influence of electronic, structural and physicochemical

properties of catalysts on the catalytic performance were understood through various characterization techniques.

2.Experimental Details

2.1 Synthesis of Catalysts

Synthesis of Co_Sm_2O_3 *from* Sm_2Co_7 *and* $SmCo_5$ *IMCs:* Sm_2Co_7 and $SmCo_5$ IMC in powder form were obtained from Sigma Aldrich and Alfa Aesar, respectively. The IMCs were heated to 550 °C for 12 h in static air and were designated as Sm_2Co_7_550 and $SmCo_5$_550. Finally, these were reduced with 10 %H_2/ Ar with 50 ml/min flow rate at 550 °C (2°C/min) for 8 h. Thus, obtained final catalysts were designated as Sm_2Co_7_550_H_2 and $SmCo_5$_550_H_2 (Scheme 1)

To compare with IMC derived catalysts, we also synthesized another series of catalysts with similar compositions by hydrothermal route. Co_Sm_2O_3 with the following Sm:Co = 2:7, 1:5, 5:7 ratios were synthesized by two different routes as given below.

Synthesis of Co_Sm_2O_3 *by Hydrothermal Route-1(HT1):* A solution was prepared by adding stoichiometric amount of $Sm(NO_3)_3.6H_2O$ and $Co(NO_3)_3.6H_2O$ in 10 ml of deionized water. This solution was then quickly added to an autoclave (capacity 60 ml) containing 20 g of NaOH in 30 ml of deionized water.[32] This quick addition resulted in precipitation of both metal hydroxides simultaneously. The autoclave containing the principate was heated to 120 °C for 24 h and then cooled down to room temperature. The obtained principate was washed with 1 L of deionized water, filtrated and dried at 120 °C for 12 h. Finally, it was heated to 550 °C in static air followed by reduction in 10 %H_2/ Ar at 550 °C for 8 h. The samples were named as Sm_5Co_7_HT1, Sm_2Co_7_HT1, $SmCo_5$_HT1.

Synthesis of Co_Sm_2O_3 *by Hydrothermal Route-2 (HT2):* In a typical synthesis, stochiometric amounts of $Sm(NO_3)_3.6H_2O$ and $Co(NO_3)_3.6H_2O$ were dissolved in 100 mL of deionized water.

The resulting solution was stirred in an oil bath at 65 °C for 3 h followed by titration with an alkaline solution (100 mL) containing NaOH (0.5 M) and Na_2CO_3 (0.1 M). Further titration is continued with NaOH (0.5 M) solution until the resulting solution reaches the pH of 12. The slurry was then transferred into a 500 mL polyethylene bottle and heated to 100 °C for 24 h in an oven.[7] The obtained solid was then filtered and washed with deionized water several times followed by drying at 120 °C for 8 h. Finally, the powder was heated to 550 °C in static air followed by reduction in 10 %H_2/ Ar at 550 °C for 8 h. The samples were named as Sm_5Co_7_HT2, Sm_2Co_7_HT2, $SmCo_5$_HT2.

Among the two different hydrothermal routes, Co_Sm_2O_3 synthesized by HT2 route possessed targeted composition of Co/Sm as seen from EDAX elemental composition (Table 1). For HT1 method a slightly lower Co/Sm ratio was observed compared to targeted composition likely due to an incomplete precipitation of Co. HT1 route was adopted to achieve a uniform distribution of Sm_2O_3 and Co in the catalyst with the idea that adding rapidly metal salt solution to NaOH would precipitate both Sm and Co simultaneously. In case of HT2, delayed addition of NaOH to metal salt solutions is expected to result in precipitation of Sm first and then Co.

Synthesis of Co_Sm_2O_3 *by* $SmCoO_3$ *Perovskite:* $Sm(NO_3)_3 \cdot 6H_2O$, $Co(NO_3)_3 \cdot 6H_2O$ were dissolved in 100 mL of deionized water, and then citric acid was added.[33] The molar ratio of total metal ions to citric acid was maintained to 1:1.5. The homogeneous solution was subjected to evaporation at 80 °C with continuous stirring to form a transparent purple hydrogel, finally dried at 120 °C for 12 h. Then, obtained gel was calcined at 800 °C for 4 h to obtain the targeted perovskite structure. The catalyst is named $SmCoO_3$.

Synthesis of Co_3O_4_Sm_2O_3: All the Co_Sm_2O_3 obtained by the above methods were heated to 600 °C in air to form Co_3O_4_Sm_2O_3. Theus, obtained all the catalysts so obtained were named by adding suffix 600 at the end of catalyst name. Example Sm_2Co_7_550_H_2 after oxidation at

View Article Online
DOI: 10.1039/D1CY01956B

600 °C is named as Sm_2Co_7_550_H_2_600. For the clarity, a schematic presentation of all the synthesized methods is given in **Scheme 1.**

2.2. Characterization of Catalyst

X-ray diffraction (XRD) measurements of the solid samples were performed with a Siemens D5000 diffractometer using the K_α radiation of Cu ($\lambda = 1.5418$ Å). The 2θ range (5– 80°) was recorded at a rate of 0.02° s^{-1}. Specific surface area of all the catalysts were determined by N_2 Physisorption at 77 K using a Micrometrics 3flex.[34] Before the analysis, samples were degassed overnight under vacuum (6.7 Pa) at 200 °C. The specific surface area was calculated from adsorption isotherm using Brunauer-Emmet-Teller (BET) method. CO chemisorption measurements were performed using Micromeritics Pulses Chemisorb 2705 apparatus. Before the analysis, catalysts were pre-treated at 550°C for 2 h under H_2 gas flow of 30 mL min^{-1}. For the analysis, CO pulses of known volume (185 µl) were consecutively injected into the He stream flowing through the catalyst (400 mg) at 35°C. After each injection, the apparatus gave a peak area (Ap) corresponding to the non-adsorbed CO. When the surface was saturated, the peak area reached the maximum (Amax), which corresponds to the volume of the CO injected (V_{CO}). To correlate the moles of non-adsorbed CO with the peak area, a calibration factor is calculated and moles of adsorbed CO per gram of catalyst was calculated. To evaluate the basicity of the prepared catalysts, CO_2-TPD experiments were conducted using a CATLAB instrument as reported earlier.[35] For TPR-H_2, before the analysis 150 mg of the catalyst was treated in air (30 ml/min) for 2 h. Then catalyst was cooled down to 70 °C and further heated with ramp rate of 10 °C/min to 700 °C in a flow of 5% H_2 in argon (30ml/min). Finally, H_2 consumed was detected using CATLAB instrument with QGA mass spectrometer. SEM-EDAX images were taken with a JEOL 7600 F with a 15 kV voltage to study the morphology and elemental composition.[34] Scanning Transmission Electron Microscopy (STEM) imaging was performed using a TEM/STEM FEI Talos F200X G2 microscope (Thermo Fisher

Scientific, Waltham, MA, USA) equipped with a high-angle annular dark-field (HAADF) detector and operated at 200 kV with a camera length of 11.5 cm. XEDS mappings were performed using the 4 Super-X detector system integrated in the equipment. The beam current and the dwell time per pixel were 130 pA and 128 μs, respectively. To improve the visual quality of the elemental maps obtained, these were filtered using a Gaussian blur of 0.8 using Velox software. X-ray photoelectron spectroscopy (XPS) measurements were carried out with a SSX 100/206 spectrometer from Surface Science Instruments as reported earlier.[36] When required, spectra were decomposed with the Casa XPS program (Casa Software Ltd., UK) with a Gaussian/Lorentzian(85/15) product function after subtraction of a nonlinear baseline. For the quantification of the elements, the sensitivity factors and acquisition parameters provided by the manufacturer were used. The binding energy scale was calibrated taking the carbon C1speak fixed at 284.8 eV as reference.[36]

Synchrotron X-ray powder diffraction experiments were performed at the XRD1/Xpress beamlines of the Elettra-Sincrotrone Trieste, Italy. A Pilatus2M detector is used for the data collection with well powdered samples tightly filled inside 200-micron glass capillaries. Wavelength used for the data collection was 0.7 Å. The X-ray absorption spectroscopy (XAS) data at the Co K edge were collected in quick-EXAFS transmission mode at the CLÆSS beamline [37] of the ALBA Synchrotron Light Source. The synchrotron radiation emitted by a multipole wiggler was first collimated vertically by a first mirror and then monochromatized with a liquid nitrogen cooled Si(311) double crystal. The monochromatized X-ray beam was then focused down to the sample at about 800 μm × 500 μm (H×V) by changing the radius of curvature of a vertically focusing mirror. The higher harmonics contribution to desired energies was minimized by appropriately setting the rejection angles of the two mirrors in the optical hutch. The incoming and outgoing photon fluxes were measured by ionization chambers filled with an appropriate mixture of N_2 and Kr

gases. Beamline energy was calibrated on the edge position of a cobalt foil. XAS data reduction has been performed according to a standard procedure using the DEMETER software package.[38] For each spectrum, the raw data have been normalized by calculating and subtracting pre-edge and post-edge backgrounds as low-order polynomial smooth curves. Successively the EXAFS signal has been extracted.

For the calculations of adsorption energies and reaction paths the DFT method was used. DFT calculations have been performed using the VASP program.[39, 40] Precisely the PBE exchange-correlation functional was used.[41] The basis set contains plane waves with a kinetic energy up to $E_{\_cut\text{-}off} = 400$ eV. The atomic structure of the surfaces has been optimized by static relaxations using a *quasi*-Newton method and the Hellmann-Feynman forces acting on the atoms. Transition states of molecular reactions were determined using the nudged elastic band method [42] and the dimer method.[43] For the structural optimizations and transition-state searches, convergence criteria of 10^{-4} eV for total energies and 0.05 eV/Å for forces acting on the atoms have been applied.

Surface calculations have been performed for slab models. The surface area of the computational cell representing the flat fcc Co (111) surface has dimensions of 7.327 Å x 8.461 Å. The slab consists of 4 atomic layers with fixed coordinates of the atoms in the bottom layer, altogether 48 atoms in the computational cell. Periodically repeated slabs are separated by a vacuum layer of 15 Å. Total energies of complexes adsorption were calculated using a 5 x 4x 1 k-point mesh for Brillouin-zone integration. The computational cells representing the surface step and the surface edge have dimensions of 7.327 Å x 16.922 Å and consist of 84 and 108 atoms, respectively. The binding energies E_b of reactants is calculated with respect to the clean surface and the reactants molecules in the gas state.

View Article Online
DOI: 10.1039/D1CY01956B

2.3. Catalyst Testing

NH_3 synthesis reaction was carried out in a fixed-bed tubular reactor. The reactor consists of a frit over which 0.2 g of catalyst was loaded.[44] This pre-treatment was performed *in situ* under 75 %H_2/N_2 (60 ml flowrate) by heating the catalyst bed to 500 °C at the rate of 10 °C/min for 2 h. Reaction tests were subsequently performed in flowing gas mixture (60 ml/min, NTP). Effluents were analysed online by gas chromatography equipped with a molecular sieve coated capillary column (CP molsieve 5Å, Varian) for NH_3 separation, an 80/100 Hayesep Q packed column 11119 Chrompack) for N_2 and H_2 separation and two thermal conductive detectors. Gas Samples for analysis were taken every 30 minutes. The NH_3 was quantified by help of multipoint calibration curve created by injecting different concentrations of NH_3 into the reactor. The catalysts were tested in the dry reforming of butane reaction in an automated six-flow parallel reactor system. Typically, 100 mg of catalyst in the form of pellets (1–0.71 mm) were placed in the reactor. A stoichiometric ratio of reactants (CO_2/C_4H_{10}=4:1) and atmospheric pressure were used for all the tests. The reactants were diluted in 80% Ar. The butane/CO_2 conversion selectivity for CO/H_2 and carbon balance (C_{out}/C_{in}) were determined as reported earlier. [31] CO and H_2 were the main products, while trace amounts of 1-butene, 2-butene, 1,3-butadiene and ethane were also detected. The carbon balance remained between 99% and 93%.

3.Results and discussion

3.1. Structural and textural characterization of Catalysts

The XRD patterns of Sm_2Co_7 and $SmCo_5$ IMCs are as shown in the **Figure 1.** The low energy XRD (with Cu K_α source) of Sm_2Co_7 shows pure rhombohedral phase. However, synchrotron high energy XRD revealed that there exists a small amount of hexagonal phase also (**Figure S1).** Sm_2Co_7 IMC crystallized in the high temperature rhombohedral phase with Gd_2Co_7 type structure ($R\bar{3}m$ space group). Sm_2Co_7 structure consists of double layers of hexagonal structure

blocks of $SmCo_5$ alternating with double layer of $SmCo_2$ cubic blocks along the common hexagonal axis ($SmCo_5$+$SmCo_2$ =Sm_2Co_7) as seen from **Scheme 2**. $SmCo_5$ IMC crystallizes in the hexagonal Ce_2Ni_7 phase with $P6_3/mmc$ space group. (**Figure S1**)

Decomposition of Sm_2Co_7 and $SmCo_5$ IMC occurs at 550 °C in air with the formation of Sm_2O_3 and Co_3O_4. XRD patterns of Sm_2Co_7_550 and $SmCo_5$_550 exhibit intense peaks at 2θ=31.2°, 36.5°, 38.6°, 44.7°, 55.3°, 59.4°, and 65.2°, which correspond to (220), (311), (222), (400), (422), (511) and (440) planes of Co_3O_4 with spinel (fcc) structure. **(Figure 1)** Diffraction peaks of Sm_2O_3 were not well resolved by low energy XRD, but synchrotron XRD pattern clearly confirms the existence of Sm_2O_3 phase with $C12m1$ space group (**Figure S2b & S3b**). Further reduction of Sm_2Co_7_550 and $SmCo_5$_550 in presence of H_2(10%)/Ar retains Sm_2O_3 phase and reduces Co_3O_4 to form Co_Sm_2O_3 (**Figure 1**) Co phase was identified by intense diffraction peaks at 2θ = 44.5°, 51.9° and 76.5° corresponding to the (111) (200) and (220) planes with fcc structure having $Fm\bar{3}m$ space group.

XRD patterns of Co_Sm_2O_3 synthesized by hydrothermal route such as $SmCo_5$_HT1, $SmCo_5$_HT2, Sm_2Co_7_HT1, Sm_2Co_7_HT2, Sm_5Co_7_HT1 and Sm_5Co_7_HT2 exhibits metallic Co(fcc) phase along with Sm_2O_3 crystallizing in $Ia\bar{3}$ space group. (**Figure S4, a-c**) The presence of Sm_2O_3 with $C12m1$ space group (instead of $Ia\bar{3}$) in Sm_2Co_7 and $SmCo_5$ IMC derived catalyst is attributed to the starting IMCs ordered structure. Homogeneous distribution of Sm and Co in crystal structure, sterically inhibits the free movement of Sm_2O_3 nano crystallites to form $Ia\bar{3}$ structure. **Figure S4d** clearly exhibits orthorhombic (*Pnma*) crystal phase of $SmCoO_3$ with diffraction peak at 2θ = 23.6°, 26.4°, 33.7°, 35.6°, 48.3°, and 49.9°, corresponding to (101), (111), (121), (210), (202) and (212) crystal planes.

Co K-edge EXAFS (extended x-ray absorption fine structure) of IMC derived catalysts (pure, oxidized and reduced) are analysed to obtain further atomic-scale information. The

View Article Online
DOI: 10.1039/D1CY01956B

Fourier transform (FT) magnitudes of EXAFS oscillations provide the local atomic arrangement around the photo-absorbing element, in the present case Co as shown in **Figure 2a-b**. Both $SmCo_5$ and Sm_2Co_7 samples are characterized by a prominent peak centred around 2 due to the Co-metal photoelectron scattering. Upon heating to 550 °C, this prominent peak disappears with the concurrent appearance of three peaks in the 0.8 to 3.2 Å range. This local atomic distribution is having a one-to-one correspondence with that of the standard Co_3O_4. This clearly indicates that the high temperature treatment led to the oxide formation involving Co-O bonds and a significant local structure modification. Upon further reduction in H_2/Ar treatment, the local structure further modifies for both the systems with the disappearance of the three-peak structure in the 0.8 to 3.2 Å with a prominent peak around 2 Å. This indicates the appearance of new Co-metal atomic bonds, with reduced atomic disorder at local scale compared to the starting $SmCo_5$ and Sm_2Co_7 IMCs. Obviously, the above local atomic changes have also a significant impact on the electronic structure which can be readily probed by the XANES (X-ray absorption near edge structure) spectroscopy. The Co K-edge XANES spectra are shown in **Figure 2c-d** for the two sets of IMCs. For a ready comparison, in both cases, the XANES spectrum of the Co_3O_4 is also included. The Sm_2Co_7 and $SmCo_5$ samples have an intense peak-edge peak (around 7710 eV) and the absorption edge is shifted to lower energies. This is similar to the typical metallic foils, indicating a relatively metallic nature of the measured samples. The high temperature treatment at 550 °C brings the system close to the oxide nature with a prominent decrease in the prepeak intensity and a significant increase in the absorption peak intensity, indicating a spectral weight transfer due to the reduction in the occupied density of states close to Fermi level and thus the appearance of the insulating character. Further H_2 treatment brings back the spectral features close to the pure IMC, however with notable differences further indicating the different electronic structure of the

IMCs and IMCs treated with air and H_2. The above results further confirm the decomposition of Sm_2Co_7 and $SmCo_5$ IMCs occurred not only on the surface but also in the bulk.

SEM images of Sm_2Co_7 IMC are presented in **Figure 3a**. Sm_2Co_7 IMCs show irregular particles with rough edge/step surfaces having average particle size of 10-40 μm. EDAX and elemental mapping confirm uniform distribution of Sm and Co in the particle with Sm:Co atomic percentage of 2:7. Even after oxidation (Sm_2Co_7_550) and reduction (Sm_2Co_7_550_H_2) of Sm_2Co_7 IMC, particle size remained almost similar (5-40 μm) with homogeneous distribution of Sm and Co.**(Figure 3b and c)** SEM images of $SmCo_5$ IMC derived catalyst also displayed similar properties as observed for Sm_2Co_7.(**Figure S5**) SEM images, colour mapping and EDAX spectra of all the Co_Sm_2O_3 catalysts synthesized by hydrothermal method exhibits spherical particles of size 1-50 um.(**Figure.4**) $SmCoO_3$_H_2 exhibits joined particles which are clustered together, forming a highly porous microstructure composed by sheet-like fragments. It was difficult to evaluate precisely the particle sizes from these pictures. (**Figure S6b**) The amount of Sm and Co determined EDAX spectra of all the catalysts are tabulated in **Table 1.**

Differences in XRD peak broadening of Sm_2Co_7, $SmCo_5$, Sm_2O_3, Co_3O_4 and Co phases in **Figure 1** indicate the presence of small crystallites of different sizes. The average crystallite sizes of Sm_2Co_7, $SmCo_5$, Sm_2O_3, Co_3O_4 and Co phases in all the catalysts were determined by Scherrer equation. (**Table S1)** Sm_2Co_7 and $SmCo_5$ IMCs show sharp XRD peaks with crystallite size of 34 nm and 29 nm respectively. But IMCs after oxidation and reduction exhibit relatively broad peaks of Sm_2O_3, Co_3O_4 and Co, showing presence of fine crystallite domains of size 5-20 nm. Consequently, particles observed by SEM are polycrystalline in nature and each particle contains a large number of nano crystallites.

To understand the morphology and structure of these nano crystallites, TEM analysis of Sm_2Co_7 and $SmCo_5$ derived catalysts were performed. TEM images of pure Sm_2Co_7 and

$SmCo_5$ were not possible to capture due to highly dense particle size, but TEM images of oxidized and reduced IMCs were measured successfully. Low magnification TEM images of Sm_2Co_7_550 confirm the presence of Co_3O_4 and Sm_2O_3 nano crystallites of size 5-20 nm as depicted in **Figure 5(a).** The high resolution (HR) TEM image exhibited distinct lattice fringes with a d-spacing of 0.46 nm and 0.31 nm corresponding to (111) and (111)/(401) plane of spinel Co_3O_4 and Sm_2O_3 structures, respectively (**Figure 5b).** Elemental colour mapping of Sm_2Co_7_550 further shows uniform distribution of Sm and Co in the particles as seen from **Figure 5c and Figure S7.** This clearly indicates that a complete decomposition of ordered Sm_2Co_7 IM occurs to form nano crystallites. TEM images of Sm_2Co_7_550_H_2 show interconnected nano crystallites of metallic Co and Sm_2O_3. The average nano crystallites size was in the range of 15-50 nm **(Figure 5d).** HR TEM images show d spacing of 0.20 nm and 0.31 nm assigned to the (111) plane of fcc(Co) and (111)/(401) plane respectively **(Figure 5e).** Colour mapping of particle further confirms the retention of uniform spreading of Sm and Co even after reduction. We also observed Sm and Co in a few smaller particles with uneven distribution. **(Figure S8)** This distribution may be possible only in the very small particle size of less than 1 μm as spotted by TEM, but most of the particles are bigger in size with average size ranging from 5-50 μm (SEM). Therefore, we believe that more even distribution of Sm_2O_3 and Co is retained within the particle of Sm_2Co_7_550_H_2. It is thought-provoking to note the presence of nano pores in Sm_2Co_7_550_H_2 catalyst compared to Sm_2Co_7_550. These nanopores might be generated during the reduction of Co_3O_4 to Co with diffusion of water molecules within the particle. TEM images of $SmCo_5$_550_H_2 exhibit comparable particle size distribution and morphology as observed for Sm_2Co_7_550_H_2 (**Figure S9**).

TEM images of Sm_2Co_7_HT1 and Sm_2Co_7_HT2 are shown in **Figure 6.** Sm_2Co_7_HT1 exhibits interconnected spherical or ovoid particles of Sm_2O_3 and Co with average particle size of 50-200 nm. (**Figure 6**) Sm_2Co_7_HT2 displays a quite different morphology with presence

of rod and spherical particles. The HAADF elemental colour mapping indicated that rods are Sm_2O_3 particles with 400-1000 nm length and 50-150 nm in diameter along with wide spread spherical Co particles of size 50-500 nm. HADDF TEM images of $SmCo_5$_HT2 also indicate the Co particles (100-400nm) dispersed in the interconnected Sm_2O_3 particle of size 50-400 nm. **(Figure S10)** The TEM image of $SmCoO_3$ after reaction shows the presence of small and uniform Co(0) dispersed in Sm_2O_3 matrix. **(Figure S6c)** In summary, uniform dispersion of Sm_2O_3 and Co nano crystallites were observed in IMC and perovskite derived catalysts compared to hydrothermal method.

In order to confirm the presence of pores, N_2 physisorption isotherm of Sm_2Co_7 and $SmCo_5$ derived catalysts were measured as shown in **Figure 7**. Sm_2Co_7/$SmCo_5$ IMC and oxidized Sm_2Co_7_550/$SmCO_5$_550 exhibit low specific surface area of ~1 m^2/g. But reduced Sm_2Co_7_550_H_2/$SmCO_5$_550_H_2 catalysts possessed higher specific surface area of ~11-13 m^2/g with type IV isotherm. This confirms the presence of nanopores between interconnected crystallites of Co and Sm_2O_3. Co_Sm_2O_3 catalysts synthesized by hydrothermal route exhibited surface area of 6 to 20 m^2/g as seen from **Table 1 and Figure S11.**

To understand the oxidation state and surface properties, XPS studies were performed on all the Co_Sm_2O_3 catalysts. (**Figure 8 & Figure S12**) The peaks of Sm 3d, Co 2p, and O 1s can be observed in the survey scan of all the catalysts. XPS spectra of Sm_2Co_7 and $SmCo_5$ IM derived catalysts are shown in **Figure 8.** The Co $2p_{3/2}$ peak of all the catalysts were deconvoluted into 3 contributions. The peak at around 778.0 eV is ascribed to the metallic Co (0). The peak centered at 780.0 eV is due to mixed Co (II, III) states and peaks centred at 785 and 789 eV are satellite peaks due to CoO and Co_3O_4 respectively.[45] IMCs show only a weak Co (0) component with a much heavier weight for the Co(II, III) components. This is due to the thin surface oxide layer present in the samples. **(Figure 8 a&d)** Reduced Sm_2Co_7_550_H_2 and $SmCo_5$_550_H_2 exhibited a peak of metallic Co (0) along with that of Co in Co_3O_4. (**Figure**

8 c&f) The XPS spectrum of Sm $3d_{5/2}$ was very similar for all the catalysts.[46] The main peak at 1082.5 eV is related to the Sm(III) and the tailing toward lower binding energy is probably due to shake off effect and not to the reduced Sm(II) species.**(Figure 8 g)** Sm_2Co_7/$SmCo_5$ IMCs, their oxidized and reduced forms certainly show variation in O 1s spectra.**(Figure 8 h-i)** Sm_2Co_7 and $SmCo_5$ IMCs show intense peak at 531.5 eV due to surface adsorbed oxygen species along with very low intense peak at 529.5 eV due to lattice oxygen (of surface oxides Co and Sm).[47] The moment IMCs are oxidized, high intense peak shifts from 531.5 eV to 529.5 eV indicating the IMCs are decomposed to respective oxides as supported from XRD. These oxides are less susceptible for the adsorption of surface O_2, hence low intensity for the peak at 531.5 eV. Further reduced catalysts exhibited, peaks at 529.5 eV and 531.5 eV with similar intensities due to the presence of lattice oxygen of Sm_2O_3 and surface oxygen adsorbed on metallic Co, respectively. The surface composition (Co/Sm) for the IMC and perovskite derived catalysts was around 2.4 and 1 respectively. (**Table 1**) However, for all the HT synthesized catalysts Co/Sm ratios were different due to the uneven distribution Co and Sm_2O_3 particles as supported by TEM.

To reveal the impact of Sm content on the reduction properties of $Co^{+3/+2}$ in Sm_xCo_y catalysts, temperature programmed reduction (TPR) was carried out. The deconvoluted H_2-TPR profiles of all the Co_Sm_2O_3 catalysts are shown in **Figure 9** and TPR peaks are summarized in **Table S2.** The peak can be deconvoluted into 3 components, namely α, β and γ.[48] The α component for all the catalysts is in the range of 320-360 °C and is mainly due to the reduction of Co_3O_4 to CoO. The β component observed in the temperature range of 360-420 °C is due to the reduction of CoO particles (coming from Co_3O_4 reduction and/or present in an amorphous/crystalline phase) to Co. Finally, the γ component is assigned to the reduction of CoO and/or Co(II) ions interacting with Sm_2O_3.[48] The shift in the reduction temperature for α and β components were not systematic with Sm content. However, γ component exhibits

a systematic increase of the reduction temperature with Sm content. Based on TPR peaks maxima the following reducibility order is obtained $SmCo_5$(400 °C)<Sm_2Co_7(420-470°C)<Sm_5Co_7(500°C). This undoubtedly confirms that Sm content increases theinteraction of Co(II/III) with Sm_2O_3. The $SmCo_5$/Sm_2Co_7 IMC derived catalyst showed higher reduction temperature for γ component (446/471 °C) compared to $SmCo_5$_HT1 (400 °C), $SmCo_5$_HT2, (399 °C), Sm_2Co_7_HT1 (417 °C). Strangely Sm_2Co_7_HT2 exhibited γ component at 471 °C indicating SMSI. This could be due to the presence Sm_2O_3 with rod like morphology interacting with spherical Co particles. TPR-H_2 confirms that metal (Co) support (Sm_2O_3) interaction is superior in IMC derived catalysts compared to HT synthesized ones.

In order to investigate the basicity of Co_Sm_2O_3 catalysts, temperature programmed desorption (TPD) of CO_2 were measured as shown in **Figure 10.** The CO_2-TPD profiles of all the catalysts exhibited major peak at 350 °C along with a shoulder at 150 °C due to the medium and weak basic sites, respectively. The strength of basic sites remains the same, but number of basic sites varied with the catalyst composition as seen from **Table.1.** As Sm_2O_3 content increases, the number of basic sites increased as seen from $SmCo_5$(45-63 μmoles) and Sm_2Co_7 (72-98 μmoles) series of catalysts. Sm_5Co_7 catalysts with high Sm content exhibited quite lower number of basic sites due to the lower surface area.

3.2. Catalytic Activity in NH_3 Synthesis and butane dry reforming

NH_3 Synthesis: Before screening the IMC derived catalysts, we tested NH_3 synthesis reaction over pure Sm_2Co_7 and $SmCo_5$ IMCs. Both IMCs were active in the reaction, even at lower temperature of 350 °C as seen from the **Figure 11a**. The calculated activation energy was very low around ~55 kJ/mol. (**Figure 11b**) Analogous activation energy value (~50 kJ/mol) was reported for Ni/LaN formed by surface decomposition of bulk $LaNi_5$ IMC.[17] The presence of LaN assisted in different reaction mechanisms for NH_3 synthesis with low activation energy.

In order to check if formation of SmN is possible with Sm_xCo_y IMCs, we measured the XRD, XPS(N1s) and EDAX of the catalyst before and after reaction. The XRD pattern of the IMCs after reaction shows complete destruction of IM structure with the formation of SmO or SmN and metallic Co. **(Figure 11c-d)** Distinguishing SmO and SmN by XRD was difficult due to similar structure, hence XPS N1s peak of both the IMCs after reaction was measured. (**Figure S13**) Sm_2Co_7 IMC after reaction exhibited 0.6 % N (mol%), whereas $SmCo_5$ exhibited no peak for N1s as seen from **Figure 11(e-f).** As a counterpart for $LaNi_5$ IMC, the surface destruction resulted in 8.6% N (mol%). This value is very high compared to 0.6% of N after complete destruction of Sm_2Co_7 IMC. Presence of very low N1s for Sm_2Co_7 could hint towards the formation oxynitride (SmO_xN_{1-x}) which catalyses NH_3 synthesis with low activation energy. But, $SmCo_5$ without any N content exhibited similar activation energy. EDAX analysis shows no N content in both the catalysts after reaction. This indicates the role of SmO in activation of N_2 with low activation energy. Formation of such a metastable SmO phase is only possible due to the controlled oxidation of IMC (limited surface adsorbed O_2 and H_2O). SmO being basic in nature efficiently enhances electron density on Co particles as result and exhibits very low activation energy of ~55 kJ/mol.

Rates of ammonia synthesis at 500 °C and 0.4 MPa over all the Co_Sm_2O_3 catalysts derived from IMC and HT routes are given in **Table1.** NH_3 synthesis rates and TOF for IM derived catalysts are much higher than those synthesized by HT method. (**Figure 12a**) For HT synthesized catalysts NH_3 synthesis rate increased with increase of Sm content (Sm:Co) from 1:5 to 2:7, but further increase of Sm content (5:7) decreased the activity. This low activity of Sm_5Co_7_HT is due to the lower surface area and a smaller number of surface Co active sites (as inferred from CO chemisorption). Nevertheless, Sm_5Co_7_HT catalyst exhibited higher TOF value compared to $SmCo_5$_HT and Sm_2Co_7_HT catalysts due to the strong metal-support interaction (as seen from TPR-H_2). Therefore, the presence of surface-active Co, amount of

Sm_2O_3 and metal-support interaction are the main causes for the difference in catalytic activity between these catalysts. The low Co/Sm ratio reduces the number of Co active sites on the surface hence low, NH_3 synthesis rate for Sm_5Co_7_HT and $SmCoO_3$_H_2. **(Table 1)** Whereas, in case of high Co/Sm ratio (0.36), the number of the Co active sites on the surface are large but possesses weak metal-support interaction as seen for $SmCo_5$_HT. In case of Sm_2Co_7_HT an optimum ratio Co/Sm~0.26 is reached with as result the higher NH_3 synthesis rate observed compared to Sm_5Co_7_HT and $SmCo_5$_HT.

Figure 12b clearly suggests that the IMC derived catalysts are active for NH_3 synthesis even at a temperature as low as 360°C compared to other catalysts. The apparent activation energies (E_a) calculated for Co_Sm_2O_3 catalysts by Arrhenius plot are shown in **Figure 12c.** The E_a values decrease in the following order Sm_2Co_7_HT1(119 KJ/mol) > $SmCo_5$_HT2(115 kJ/mol) > $SmCo_5$_HT1(110 kJ/mol) > Sm_2Co_7_HT2(107 kJ/mol)> $SmCo_5$_550_H_2 (81 kJ/mol) > Sm_2Co_7_H_2 (77 kJ/mol). The IMC derived catalysts exhibited activation energy much lower than hydrothermally synthesized ones, implying that the NH_3 synthesis is promoted over the IMC derived catalysts. NH_3 synthesis rate of Sm_2Co_7_550_H_2 at 500 °C and 0.4 MPa was 3.7 mmol NH_3/g/h compared to other catalysts and no deactivation for 72 h confirms, potential thermal stability of the catalyst in long run. (**Figure 12d**) XRD of fresh Sm_2Co_7_550_H_2 and recycled catalysts shows no change on the patterns, showing retention of both phases even after reaction. The SEM images of recycled catalyst shows similar particle morphology and uniform distribution of Sm_2O_3 and Co **(Figure 13)** The XPS also exhibits metallic Co as observed for the fresh catalyst suggesting the catalyst is highly stable under these reaction conditions.

The reaction order for N_2 (α), H_2 (β)and NH_3 (γ) was determined to understand the reaction mechanism and the results are shown in **Figure 14a-c.**[49] The N_2 order for Sm_2Co_7_550_H_2 and Sm_2Co_7_HT2 catalysts was almost equal to 1 suggesting, rate determining step is dissociation of N_2 molecule.[20] The reaction order of H_2 was positive (0.8

and 1.23) indicating no poisoning of cobalt surfaces by H_2 and the possible help that Co provides in the activation of N_2 at low temperature. The positive value for NH_3 reaction order indicates that the reaction rate is not slowed down by produced NH_3. This is due to the presence of high number of basic sites that will help in easy desorption of NH_3. Furthermore, we confirmed that reaction rate over Sm_2Co_7_550_H_2 exhibits approximately linear response to the pressure increase, showing that the catalyst does not suffer from H_2 and NH_3 poisoning even at high reaction temperature of 500 °C. (**Figure 14d**)

The high catalytic activity of IMCs derived catalysts compared to HT ones is associated with stronger metal support interaction, smaller crystallite size, and morphology of particles. IMCs derived catalysts, possess evenly distributed Sm_2O_3 and Co nano crystallites that are well packed within a bigger particle and that have improved strong metal (Co)-support (Sm_2O_3) interaction. For HT synthesized catalyst both Sm_2O_3 and Co particles are segregated as particles (as seen from TEM images) hence a weak metal support interaction. TPR-H_2 also supports SMSI for IMC derived catalyst compared to HT ones as discussed earlier. This SMSI enhances electron density on cobalt particle, which in turn enhances the electron density in the antibonding orbitals of adsorbed N_2 molecules and activates them by reducing the bond order.[18]

Perovskite being ordered structure, should result in similar catalytic activity as that of IMC derived catalysts. $SmCoO_3$_H_2 with higher Sm content and uniform distribution of Co and Sm_2O_3 exhibits low NH_3 synthesis rate and high activation energy (105 kJ/mol) compared to IMC derived catalysts. This indicates that along with the electronic factors the structural effect also plays an important role in NH_3 synthesis. Since, NH_3 synthesis is a structure sensitive reaction, high activity of IMC derived catalysts could also be due to the particle morphology. Reaction order studies suggest that N_2 activation is the rate determining step in the reaction. The Sm_2Co_7_550_H_2 and $SmCo_5$_550_H_2 particles exhibit non-uniform surfaces

with several edges, steps and cracks as seen from SEM/TEM images (**Figures 3&5**) and these geometries could activate N_2 with lower activation energy. At the opposite, very smooth and soft surface morphologies are observed in case of $SmCoO_3$_H_2 (for HT catalysts too), which require high energy for N_2 activation. (**Figures 4&6**) The intense peak in XRD and TEM images suggest that Co (111) is the exposed plane in all the catalysts and brings plausible active sites for the NH_3 synthesis.

In order to understand this structural effect, adsorption, activation and dissociation barrier of N_2 on different Co (111) geometries (flat, step, edge), were calculated using the Density Functional Theory.[39-43] In case of the flat Co (111) plane, the N_2 molecule prefers to adsorb on top of a Co atom in the vertical upright position (T). At this position there is no N_2 activation and its binding energy E_b to the Co(111) surface is -66 kJ/mol. To dissociate the N_2 molecule, it has to tilt to the bridge position (B). The energy barrier for tilting N_2 (T) to the bridged N_2 (B) position is 64 kJ/mol. At this position N_2 is adsorbed between two neighbouring triplet hollow sites. Both N atoms bind with the surface. At this bridge position the N_2 molecule is activated, the N-N is stretched by 15.7%. The dissociation barrier to 2N is 71 kJ/mol. The binding energy of the dissociated N atoms with respect to N_2 in the gas state is -142 kJ/mol. Total energy barrier for this two-step dissociation process between the N_2 (T) and 2N is 109 kJ/mol. (**Figure 15a**) This value shows that the clean flat (111) surfaces require rather high energy for the N_2 dissociation.

The surfaces of Co particles are mostly terminated by flat (111) planes. However, on the atomic scale the (111) surfaces can be covered by additional layers of atoms having a form of irregular islands. The boundaries of such monoatomic layers are formed by surface steps. The surface steps are also parts of (211) or other similar surfaces. While Co atoms on the flat (111) surface have coordination number of 9, the atoms in the step edge structure have coordination number of 7. The Co atoms on the step edges are thus more reactive. The N_2

View Article Online
DOI: 10.1039/D1CY01956B

molecule at the surface step does not prefer to adsorb in the vertical upright position (T) as on the flat (111) surface but prefers to adsorb into the bridge position with E_b = -100 kJ/mol. (**Figure 15b**) The N-N bond is stretched 15.0%. The calculated dissociation barrier is 78 kJ/mol. This is the total energy barrier for the whole N_2 dissociation process.

On the nm scale, the (111) planes terminating the surface of Co nanograins can have different orientations. From the viewpoint of the catalytic activity the important configuration of the surface atoms is also the edge between two (111) surfaces. On sub micrometer scale such configuration of the (111) planes can form surface steps consisting of many atomic layers. Such steps can be observed in SEM and TEM images. **Figure 16** represents the structural model with the edge between two (111) surfaces. The angle between such (111) surfaces is 109 degrees (angle between the cubic diagonals). The calculated energy barrier of N_2 dissociation adsorbed in the edge between two surface planes (**Figure 15c**) is 82 kJ/mol. The inner edge between two (111) planes can thus be also the active site for N_2 dissociation at low reaction temperatures.

Dissociated N atoms can move on the Co(111) surface rather easily. The activation energy of a diffusion jump of N between fcc to hcp hollow site is 59 kJ/mol. The energy barrier for a jump of N in the opposite direction is by 9 kJ/mol lower. In NH_3 synthesis the hydrogenation steps $NH_x+H \rightarrow NH_{(x+1)}$, x=0,1,2, must proceed on the catalyst surface. The atomic hydrogen is obtained easily. On the Co(111) surface H_2 adsorbs dissociatively. The dissociation barrier is lower than 5 kJ/mol. The adsorption energies of H in the fcc and hcp hollows are -63 kJ/mol and -64 kJ/mol, respectively. Diffusion jumps require the activation energy of 13 kJ/mol, only.

The energy profile of the complete chain of the hydrogenation steps of NH_3 synthesis on the (111) surface is presented in **Figure S14**. The calculated energy barriers of the three

hydrogenation steps of NH_x, x=0,1,2, are 95 kJ/mol, 117 kJ/mol, and 124 kJ/mol, respectively. In the energy profile of the whole reaction path the co-adsorbed H atoms shifts the energies of the hydrogenation steps deeper. The desorption energy of NH_3 molecule from the (111) surface is 87 kJ/mol.

From the viewpoint of the catalytic activity the rate determining step of the whole NH_3 synthesis process is N_2 dissociation. The structural complexity of the surface plays an important role. Morphology studies demonstrate that the surface of metallic Co(fcc) grains is nanostructured. In addition to the surface steps on the (111) surfaces there can exist also reactive high-index surfaces or other reactive surface defects (kinks, twins). These surface defects can disappear by annealing (or at high reaction temperatures) but the presence of Sm_2O_3 can stabilize the nanostructured Co. As a result, the N_2 activation goes through lower activation energy in IMC derived catalysts. It is also possible that if the Sm oxide nanoparticles are smaller than Co nanoparticles they can be more frequently joined and form larger particles with more regular flat surface areas. More regular surfaces have lower catalytic activity for N_2 dissociation as it is seen in the case of HT and $SmCoO_3$ catalysts.

Table S3. shows the comparison of catalytic activity of Sm_2Co_7 IMC derived catalyst with other reported cobalt-based catalysts. The Co_Sm_2O_3 and Co_SmO derived from Sm_2Co_7 IMC exhibits low activation energy of 77 and 55 kJ/mol, which is comparable to other reported Co based catalysts such as hydride, (LiH, BaH_2, $BaTiO_{2.35}H_{0.65}$), electride ($C_{12}A_7$: e^-, LaCoSi) and oxide (CeO_2, $LaCoO_3$). [22, 24-26,33, 50-51] Such low activation energy is due to the strong metal (Co) support (Sm2O3) interaction that has formed by decomposition of ordered IM structure. Co_Sm_2O_3 and Co_SmO catalyst exhibit comparable catalytic activity with Co/CeO_2, $LaCoO_3$, Co_3Mo_3N and $Co/BaTiO_{2.35}H_{0.65}$. The lower NH_3 yield (μmole/g/h) compared to other hydride, elctride and oxide catalysts could be due to the lower surface area of the catalyst (13 m^2/g). Moreover, each of these reported catalysts have their own Pro and

Cons related to bulk synthesis, cost of catalyst, stability, operating conditions etc. In this regard Sm_2Co_7 has already been commercially synthesized in bulk quantity due to its application in magnetics materials. Furthermore Sm1Co1 IMC could be explored in this direction, Sm:Co ration of 1 could further boost the catalytic activity. The catalytic activity in case of IMC derived catalyst can be further improved by synthesizing well dispersed nano particles of IMCs on a on high surface area support. Insights on the such new materials and their mechanisms will dig towards finding a realistic catalyst for NH_3 synthesis.

Butane Dry Reforming: All the Co_Sm_2O_3 catalysts that are active in the NH_3 synthesis showed very low activity in butane dry reforming (butane conversion <4 %). However, the same catalysts after oxidation (at 600°C) exhibited excellent catalytic activity in the reaction, indicating that Co_3O_4 are the active sites instead of metallic Co. The XRD pattern of the catalyst after oxidation are shown in **Figure S15.** The temperature screening tests showed that Co_3O_4_Sm_2O_3 catalyst derived from the Sm_2Co_7 and, $SmCo_5$ IMCs, as well as $SmCoO_3$ showed excellent butane and CO_2 conversions compared to the hydrothermally (HT) synthesized catalysts. **(Figure 17a-b)**. Both the IMC derived catalysts were active for dry reforming even below 450 °C and exhibited butane conversion of 12% and CO_2 conversion of 16% with high selectivity toward CO and H_2 (73% and 27% respectively) at 550°C. H_2/CO ratio of 0.6 was expected for 4:1 stoichiometric ratio of the reactant. But H_2/CO value of 0.3 to 0.4 is achieved in our experiments, suggesting excess production of CO and/or consumption of H_2, due to the reverse water gas shift reaction (RWGS) that also generally occurs during the dry reforming reaction. [31, 52]. It is interesting to note that at lower butane conversion (0.5-1.5%, achieved at 400-450 °C), the IMC catalysts were only selective to 2-butene and 1,3-butadiene, which indicates that at low conversion the butane dehydrogenation reaction is predominant. However, at higher temperatures and higher conversion values, the catalysts promote the butane dry reforming instead of the dehydrogenation pathway, giving CO and H_2

as the only products. This is in line with previous studies, where the competition of these two reactions was also observed. [53, 54] The long-term stability of the catalysts was tested at 550 °C for 16 h. **(Figure 17c-d)**. Both CO_2, butane conversion and CO/H_2 selectivity were stable over time, with only a slight deactivation (1.7% for butane conversion and 0.4% for CO_2 conversion) in the first 3 h of reaction. Furthermore, the carbon balance was 93%, suggesting that a low amount of carbon is deposited on the catalyst by butane cracking and/or the Boudouard reaction.

The results from **Figure 17** suggest that the Co_3O_4_Sm_2O_3 catalysts derived from the HT route are not active, probably due to the non-uniform distribution of the Sm_2O_3 and Co_3O_4 particles. A uniform distribution is well preserved in the case of IM and perovskite derived catalysts. This demonstrates that well dispersed Co_3O_4 and Sm_2O_3 active sites in close proximity are necessary for the reaction. The basic nature of Sm_2O_3 may promotes the adsorption and activation of CO_2, and Co_3O_4 for butane adsorption/activation. [55, 56]

Understanding Catalyst Properties through NH_3 and butane dry reforming reactions: Unlike in the NH_3 synthesis, Sm_2Co_7 and $SmCo_5$ IMC derived catalysts exhibited almost similar butane and CO_2 conversion in dry reforming, suggesting that there is no impact of Sm_2O_3 quantity on the activity. This means that the NH_3 synthesis reaction is controlled by the electronic effect (electron donation from Sm_2O_3 to Co), but butane dry reforming is not controlled by such electronic effects. Similarly, NH_3 synthesis is a structural sensitive reaction. Unlike in butane dry reforming, $SmCoO_3$ derived catalyst despite high amount of Sm_2O_3(Co/Sm=1) and uniform dispersion of Co and Sm_2O_3 exhibits lower catalytic activity in NH_3 synthesis compared to IMC derived catalysts. This supports that along with the electronic effect, structural effect of Co_Sm_2O_3 also influences the N_2 activation as illustrated earlier by DFT studies.

Moreover, HT synthesized catalysts, containing segregated Co_Sm_2O_3 phases and bigger Co particles, were active in NH_3 synthesis, the same catalysts after oxidation were not active in the dry reforming reaction. This means dry reforming is a structural sensitive reaction as it is controlled by geometrical factors - *i.e.,* a uniform distribution of Sm_2O_3 and Co_3O_4 sites is necessary for the high catalytic activity as discussed earlier. These studies suggest that intermetallic compounds can be excellent catalyst precursors for the synthesis of the metal/metal oxides composite catalysts that are highly active, stable and selective in heterogenous catalysis. Despite the low number of surface-active sites, Sm_2Co_7 and $SmCo_5$ derived catalysts showed promising results in activation of N_2 and CO_2 at low temperature.

4. Conclusions

In this work, we have shown that ordered intermetallic compounds (IMCs) are good precursors to prepare highly stable and active metal/metal oxide composite catalysts. The Sm_2Co_7 and $SmCo_5$ IMCs were decomposed at 550 °C in air followed by reduction in H_2, resulting in a Co_Sm_2O_3 catalyst that was active in NH_3 synthesis with low activation energy (77 kJ/mol). The Co_Sm_2O_3 catalyst exhibited a good surface area of 13 m^2/g with presence of nanopores compared to the pure IMC (1 m^2/g). The SEM/TEM characterization of Co_Sm_2O_3 exhibit particles of 5-20 μm and each of these particles contains Co and Sm_2O_3 nano crystallites of size less than 20 nm. TPR-H_2 along with DFT studies show the presence of strong metal support interaction along with several surface steps and edges of the particle, that facilitates the decomposition of N_2 molecule with low activation energy. The Co_Sm_2O_3 catalyst was highly stable and active at 450 and 550 °C under 0.4 MPa for 74 h with no loss of activity. Co_Sm_2O_3 catalyst obtained from the hydrothermal route exhibited lower TOF compared to Co_Sm_2O_3 derived from IMCs. Further oxidation of Co_Sm_2O_3 resulted in a Co_3O_4_Sm_2O_3 catalyst that is active in the butane dry reforming reaction, with significant CO_2 and butane conversion at relatively low temperature (550 °C). The uniform distribution of the Co_3O_4 and Sm_2O_3 active

sites promotes the adsorption and activation of butane and CO_2 molecules to produce syngas. Despite the low number of surface-active sites, Sm_2Co_7 and $SmCo_5$ IMCs derived catalysts provide new and exciting perspectives to attain further exploration of different wide varieties of IMCs as catalyst precursors. The systematic studies of Sm_2Co_7 and $SmCo_5$ IMC derived catalysts in NH_3 synthesis and dry reforming reaction paves the way for a rational approach to develop highly efficient and durable catalysts with potential implication in wide range of catalytic reactions.

Supplement information: Synchrotron high energy XRD of IMC derived catalyst, XRD, XPS and surface area of Co_Sm_2O_3 catalyst synthesized by hydrothermal method. Crystallite size of Sm_2O_3, Co, and Co_3O_4 of all the catalysts. SEM/HADDF-STEM images of Co_Sm_2O_3 catalysts.

Acknowledgment: Vijaykumar S.M and E.M Gaigneaux are thankful to Marie Skłodowska Curie – Individual Fellowship (MSCA-IF-EF-ST), Horizon 2020 – Research and Innovation Framework Programmed, (Project number: 841964) for funding. FRS-FNRS is also thanked for the acquisition of the nitrogen physisorption equipment used (project EQP U. N030.18). M.K. is thankful for support from the Slovak Grant Agency VEGA 2/0144/21 and from APVV 19-0369. M. Ronda-Lloret and N. Raveendran Shiju thank the Netherlands Organization for Scientific Research (NWO) for the grant "Developing novel catalytic materials for converting CO_2, methane and ethane to high-value chemicals in a hybrid plasma-catalytic reactor" (China.15.119). JJ Delgado thanks the support by MINECO (Spain) and Junta de Andalucia through projects MAT2017-86992-R and PY18-2727.

References

[1] V.S. Marakatti, S.C. Peter, Synthetically tuned electronic and geometrical properties of intermetallic compounds as effective heterogeneous catalysts, Progress in Solid State Chemistry, 52 (2018) 1-30.
[2] S. Furukawa, T. Komatsu, Intermetallic Compounds: Promising Inorganic Materials for Well-Structured and Electronically Modified Reaction Environments for Efficient Catalysis, ACS Catalysis, 7 (2017) 735-765.
[3] V.S. Marakatti, S.C. Sarma, B. Joseph, D. Banerjee, S.C. Peter, Synthetically Tuned Atomic Ordering in PdCu Nanoparticles with Enhanced Catalytic Activity toward Solvent-Free Benzylamine Oxidation, ACS Applied Materials & Interfaces, 9 (2017) 3602-3615.
[4] M. Armbrüster, Intermetallic compounds in catalysis – a versatile class of materials meets interesting challenges, Science and Technology of Advanced Materials, 21 (2020) 303-322.
[5] V.S. Marakatti, S.C. Sarma, S. Sarkar, M. Krajčí, E.M. Gaigneaux, S.C. Peter, Synthetically Tuned Pd-Based Intermetallic Compounds and their Structural Influence on the O2 Dissociation in Benzylamine Oxidation, ACS Applied Materials & Interfaces, 11 (2019) 37602-37616.
[6] V.S. Marakatti, S.C. Peter, Nickel–antimony nanoparticles confined in SBA-15 as highly efficient catalysts for the hydrogenation of nitroarenes, New Journal of Chemistry, 40 (2016) 5448-5457.
[7] V.S. Marakatti, N. Arora, S. Rai, S.C. Sarma, S.C. Peter, Understanding the Role of Atomic Ordering in the Crystal Structures of NixSny toward Efficient Vapor Phase Furfural Hydrogenation, ACS Sustainable Chemistry & Engineering, 6 (2018) 7325-7338.
[8] M. Armbrüster, R. Schlögl, Y. Grin, Intermetallic compounds in heterogeneous catalysis—a quickly developing field, Science and Technology of Advanced Materials, 15 (2014) 034803.
[9] S. Penner, P.D. Kheyrollahi Nezhad, Steering the Catalytic Properties of Intermetallic Compounds and Alloys in Reforming Reactions by Controlled in Situ Decomposition and Self-Activation, ACS Catalysis, 11 (2021) 5271-5286.
[10] M. Wu, W. Li, A.T. Ogunbiyi, G. Guo, F. Xue, K. Chen, B. Zhang, Highly Active and Stable Palladium Catalysts Supported on Surface-modified Ceria Nanowires for Lean Methane Combustion, ChemCatChem, 13 (2021) 664-673.
[11] M. Armbrüster, M. Behrens, K. Föttinger, M. Friedrich, É. Gaudry, S.K. Matam, H.R. Sharma, The Intermetallic Compound ZnPd and Its Role in Methanol Steam Reforming, Catalysis Reviews, 55 (2013) 289-367.
[12] X. Fu, Y. Liu, J. Deng, L. Jing, X. Zhang, K. Zhang, Z. Han, X. Jiang, H. Dai, Intermetallic compound PtMny-derived Pt−MnOx supported on mesoporous CeO2: Highly efficient catalysts for the combustion of toluene, Applied Catalysis A: General, 595 (2020) 117509.
[13] Y.-H. Huang, S.-F. Wang, A.-P. Tsai, S. Kameoka, Characterization of new catalysts prepared by in-situ activation of Ce50Ni50-xAux intermetallic compounds for CO oxidation, Intermetallics, 120 (2020) 106748.
[14] A. Elattar, W.E. Wallace, R.S. Craig, Hydrocarbon Synthesis Using Catalysts Formed by Intermetallic Compound Decomposition, in: Hydrocarbon Synthesis from Carbon Monoxide and Hydrogen, AMERICAN CHEMICAL SOCIETY, 1979, pp. 7-14.
[15] P.W. Menezes, S. Yao, R. Beltrán-Suito, J.N. Hausmann, P.V. Menezes, M. Driess, Facile Access to an Active γ-NiOOH Electrocatalyst for Durable Water Oxidation Derived From an Intermetallic Nickel Germanide Precursor, Angewandte Chemie International Edition, 60 (2021) 4640-4647.
[16] T. Takeshita, W.E. Wallace, R.S. Craig, Rare earth intermetallics as synthetic ammonia catalysts, Journal of Catalysis, 44 (1976) 236-243.
[17] T.-N. Ye, Y. Lu, Y. Kobayashi, J. Li, S.-W. Park, M. Sasase, M. Kitano, H. Hosono, Efficient Ammonia Synthesis over Phase-Separated Nickel-Based Intermetallic Catalysts, The Journal of Physical Chemistry C, 124 (2020) 28589-28595.

[18] V.S. Marakatti, E.M. Gaigneaux, Recent Advances in Heterogeneous Catalysis for Ammonia Synthesis, ChemCatChem, 12 (2020) 5838-5857.
[19] S. Hagen, R. Barfod, R. Fehrmann, C.J.H. Jacobsen, H.T. Teunissen, K. Ståhl, I. Chorkendorff, New efficient catalyst for ammonia synthesis: barium-promoted cobalt on carbon, Chemical Communications, (2002) 1206-1207.
[20] S. Hagen, R. Barfod, R. Fehrmann, C.J.H. Jacobsen, H.T. Teunissen, I. Chorkendorff, Ammonia synthesis with barium-promoted iron–cobalt alloys supported on carbon, Journal of Catalysis, 214 (2003) 327-335.
[21] W. Raróg-Pilecka, A. Jedynak-Koczuk, J. Petryk, E. Miśkiewicz, S. Jodzis, Z. Kaszkur, Z. Kowalczyk, Carbon-supported cobalt–iron catalysts for ammonia synthesis, Applied Catalysis A: General, 300 (2006) 181-185.
[22] X. Wang, L. Li, T. Zhang, B. Lin, J. Ni, C.-T. Au, L. Jiang, Strong metal–support interactions of Co-based catalysts facilitated by dopamine for highly efficient ammonia synthesis: in situ XPS and XAFS spectroscopy coupled with TPD studies, Chemical Communications, 55 (2019) 474-477.
[23] W. Raróg-Pilecka, E. Miśkiewicz, L. Kępiński, Z. Kaszkur, K. Kielar, Z. Kowalczyk, Ammonia synthesis over barium-promoted cobalt catalysts supported on graphitised carbon, Journal of Catalysis, 249 (2007) 24-33.
[24] P. Wang, F. Chang, W. Gao, J. Guo, G. Wu, T. He, P. Chen, Breaking scaling relations to achieve low-temperature ammonia synthesis through LiH-mediated nitrogen transfer and hydrogenation, Nature Chemistry, 9 (2017) 64-70.
[25] W. Gao, P. Wang, J. Guo, F. Chang, T. He, Q. Wang, G. Wu, P. Chen, Barium Hydride-Mediated Nitrogen Transfer and Hydrogenation for Ammonia Synthesis: A Case Study of Cobalt, ACS Catalysis, 7 (2017) 3654-3661.
[26] Y. Inoue, M. Kitano, M. Tokunari, T. Taniguchi, K. Ooya, H. Abe, Y. Niwa, M. Sasase, M. Hara, H. Hosono, Direct Activation of Cobalt Catalyst by 12CaO·7Al2O3 Electride for Ammonia Synthesis, ACS Catalysis, 9 (2019) 1670-1679.
[27] M. Ronda-Lloret, G. Rothenberg, N.R. Shiju, A Critical Look at Direct Catalytic Hydrogenation of Carbon Dioxide to Olefins, ChemSusChem, 12 (2019) 3896-3914.
[28] E. Devid, D. Zhang, D. Wang, M. Ronda-Lloret, Q. Huang, G. Rothenberg, N.R. Shiju, A.W. Kleyn, Dry Reforming of Methane under Mild Conditions Using Radio Frequency Plasma, Energy Technology, 8 (2020) 1900886.
[29] B. Yao, W. Ma, S. Gonzalez-Cortes, T. Xiao, P.P. Edwards, Thermodynamic study of hydrocarbon synthesis from carbon dioxide and hydrogen, Greenhouse Gases: Science and Technology, 7 (2017) 942-957.
[30] H.C. Hendrikse, A. van der Weijden, M. Ronda-Lloret, T. Yang, R. Bliem, N.R. Shiju, M. van Hecke, L. Li, W.L. Noorduin, Shape-Preserving Chemical Conversion of Architected Nanocomposites, Advanced Materials, 32 (2020) 2003999.
[31] M. Ronda-Lloret, V.S. Marakatti, W.G. Sloof, J.J. Delgado, A. Sepúlveda-Escribano, E.V. Ramos-Fernandez, G. Rothenberg, N.R. Shiju, Butane Dry Reforming Catalyzed by Cobalt Oxide Supported on Ti2AlC MAX Phase, ChemSusChem, 13 (2020) 6401-6408.
[32] Z. Ma, S. Zhao, X. Pei, X. Xiong, B. Hu, New insights into the support morphology-dependent ammonia synthesis activity of Ru/CeO2 catalysts, Catalysis Science & Technology, 7 (2017) 191-199.
[33] X. Wang, X. Peng, H. Ran, B. Lin, J. Ni, J. Lin, L. Jiang, Influence of Ru Substitution on the Properties of LaCoO3 Catalysts for Ammonia Synthesis: XAFS and XPS Studies, Industrial & Engineering Chemistry Research, 57 (2018) 17375-17383.
[34] V.S. Marakatti, E.M. Gaigneaux, Alkylation of resorcinol with tertiary butanol over zeolite catalysts: Shape selectivity vs acidity, Catalysis Communications, 152 (2021) 106291.
[35] S. Ramesh, F. Devred, L. van den Biggelaar, D.P. Debecker, Hydrotalcites Promoted by NaAlO2 as Strongly Basic Catalysts with Record Activity in Glycerol Carbonate Synthesis, ChemCatChem, 10 (2018) 1398-1405.

[36] V.S. Marakatti, S. Marappa, E.M. Gaigneaux, Sulfated zirconia: an efficient catalyst for the Friedel–Crafts monoalkylation of resorcinol with methyl tertiary butyl ether to 4-tertiary butylresorcinol, New Journal of Chemistry, 43 (2019) 7733-7742.
[37] L. Simonelli, C. Marini, W. Olszewski, M. Ávila Pérez, N. Ramanan, G. Guilera, V. Cuartero, K. Klementiev, CLÆSS: The hard X-ray absorption beamline of the ALBA CELLS synchrotron, Cogent Physics, 3 (2016) 1231987.
[38] B. Ravel, M. Newville, ATHENA, ARTEMIS, HEPHAESTUS: data analysis for X-ray absorption spectroscopy using IFEFFIT, Journal of synchrotron radiation, 12 (2005) 537-541.
[39] G. Kresse, D. Joubert, From ultrasoft pseudopotentials to the projector augmented-wave method, Physical Review B, 59 (1999) 1758-1775.
[40] P.E. Blöchl, Projector augmented-wave method, Physical Review B, 50 (1994) 17953-17979.
[41] J.P. Perdew, K. Burke, M. Ernzerhof, Generalized Gradient Approximation Made Simple [Phys. Rev. Lett. 77, 3865 (1996)], Physical Review Letters, 78 (1997) 1396-1396.
[42] D. Sheppard, R. Terrell, G. Henkelman, Optimization methods for finding minimum energy paths, The Journal of Chemical Physics, 128 (2008) 134106.
[43] A. Heyden, A.T. Bell, F.J. Keil, Efficient methods for finding transition states in chemical reactions: Comparison of improved dimer method and partitioned rational function optimization method, The Journal of Chemical Physics, 123 (2005) 224101.
[44] C. Fernández, C. Sassoye, N. Flores, N. Escalona, E.M. Gaigneaux, C. Sanchez, P. Ruiz, Insights in the mechanism of deposition and growth of RuO2 colloidal nanoparticles over alumina. Implications on the activity for ammonia synthesis, Applied Catalysis A: General, 502 (2015) 48-56.
[45] M.C. Biesinger, B.P. Payne, A.P. Grosvenor, L.W.M. Lau, A.R. Gerson, R.S.C. Smart, Resolving surface chemical states in XPS analysis of first row transition metals, oxides and hydroxides: Cr, Mn, Fe, Co and Ni, Applied Surface Science, 257 (2011) 2717-2730.
[46] H. Brunckova, M. Kanuchova, H. Kolev, E. Mudra, L. Medvecky, XPS characterization of SmNbO4 and SmTaO4 precursors prepared by sol-gel method, Applied Surface Science, 473 (2019) 1-5.
[47] J.-C. Dupin, D. Gonbeau, P. Vinatier, A. Levasseur, Systematic XPS studies of metal oxides, hydroxides and peroxides, Physical Chemistry Chemical Physics, 2 (2000) 1319-1324.
[48] L. Spadaro, F. Arena, M.L. Granados, M. Ojeda, J.L.G. Fierro, F. Frusteri, Metal–support interactions and reactivity of Co/CeO2 catalysts in the Fischer–Tropsch synthesis reaction, Journal of Catalysis, 234 (2005) 451-462.
[49] R. Kojima, K.-i. Aika, Cobalt molybdenum bimetallic nitride catalysts for ammonia synthesis: Part 2. Kinetic study, Applied Catalysis A: General, 218 (2001) 121-128.
[50] Y. Tang, Y. Kobayashi, N. Masuda, Y. Uchida, H. Okamoto, T. Kageyama, S. Hosokawa, F. Loyer, K. Mitsuhara, K. Yamanaka, Y. Tamenori, C. Tassel, T. Yamamoto, T. Tanaka, H. Kageyama, Metal-Dependent Support Effects of Oxyhydride-Supported Ru, Fe, Co Catalysts for Ammonia Synthesis, Advanced Energy Materials, 8 (2018) 1801772.
[51] Y. Gong, J. Wu, M. Kitano, J. Wang, T.-N. Ye, J. Li, Y. Kobayashi, K. Kishida, H. Abe, Y. Niwa, H. Yang, T. Tada, H. Hosono, Ternary intermetallic LaCoSi as a catalyst for N2 activation, Nature Catalysis, 1 (2018) 178-185.
[52] I.G. Osojnik Črnivec, P. Djinović, B. Erjavec, A. Pintar, Effect of synthesis parameters on morphology and activity of bimetallic catalysts in CO2–CH4 reforming, Chemical Engineering Journal, 207-208 (2012) 299-307.
[53] V.D.B.C. Dasireddy, M. Huš, B. Likozar, Effect of O2, CO2 and N2O on Ni–Mo/Al2O3 catalyst oxygen mobility in n-butane activation and conversion to 1,3-butadiene, Catalysis Science & Technology, 7 (2017) 3291-3302.
[54] B. Yan, X. Yang, S. Yao, J. Wan, M. Myint, E. Gomez, Z. Xie, S. Kattel, W. Xu, J.G. Chen, Dry Reforming of Ethane and Butane with CO2 over PtNi/CeO2 Bimetallic Catalysts, ACS Catalysis, 6 (2016) 7283-7292.
[55] S. Sato, R. Takahashi, M. Kobune, H. Gotoh, Basic properties of rare earth oxides, Applied Catalysis A: General, 356 (2009) 57-63.

[56] A.W. Budiman, S.-H. Song, T.-S. Chang, C.-H. Shin, M.-J. Choi, Dry Reforming of Methane Over Cobalt Catalysts: A Literature Review of Catalyst Development, Catalysis Surveys from Asia, 16 (2012) 183-197.

View Article Online
DOI: 10.1039/D1CY01956B

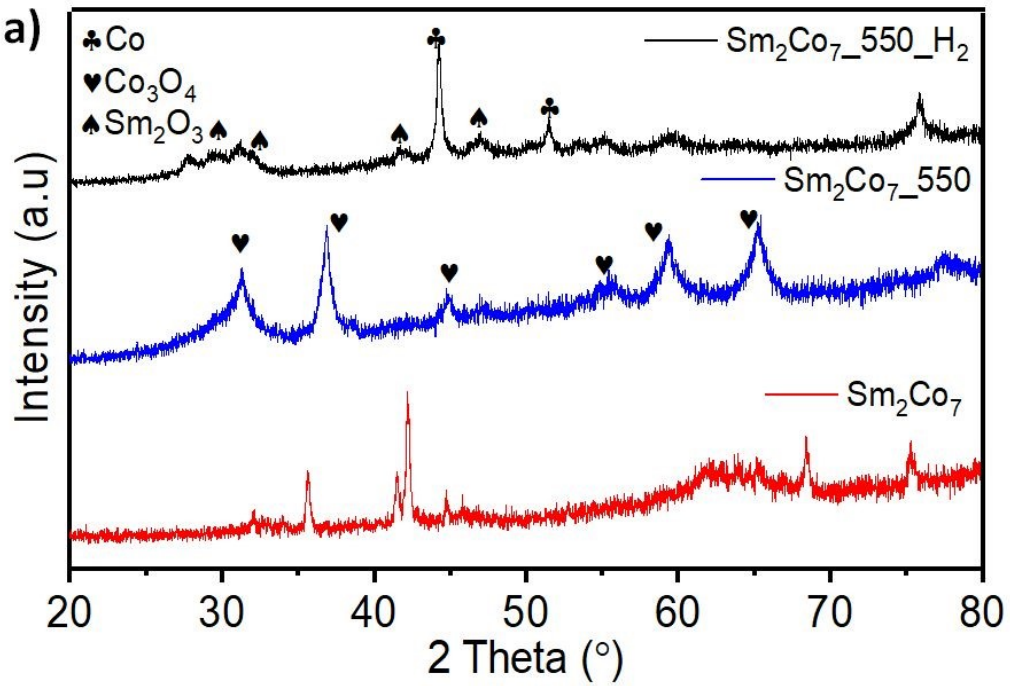

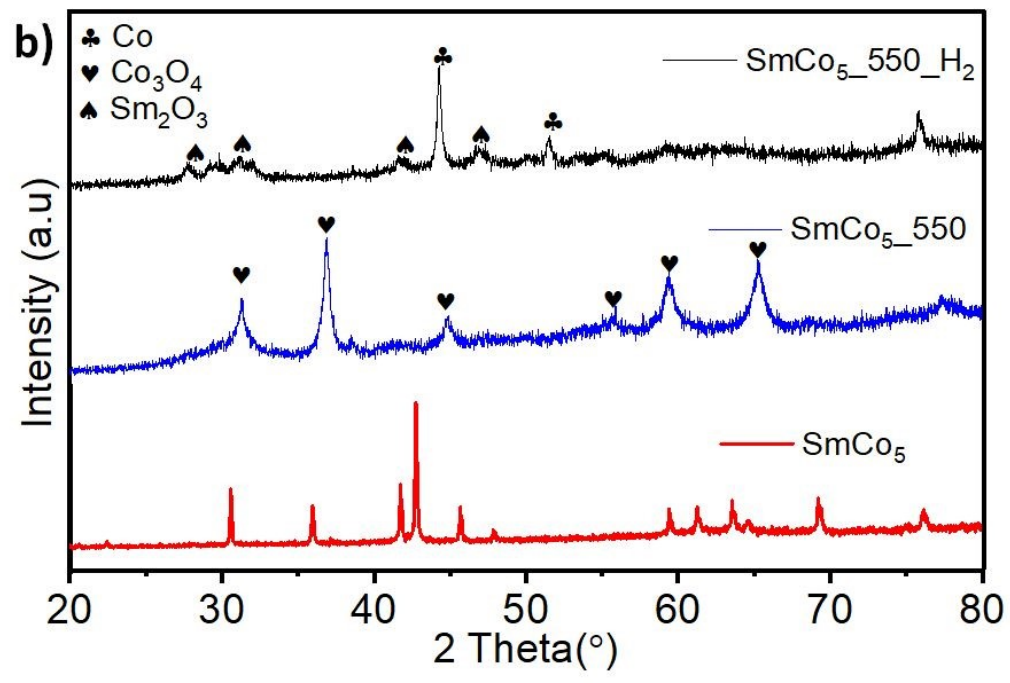

View Article Online
DOI: 10.1039/D1CY01956B

Figure 1. XRD pattern of pure a) Sm_2Co_7 and b) $SmCo_5$ Intermetallic Compounds and their phase after calcination (Sm_2Co_7_550, $SmCo_5$_550) and reducing in H_2 at 550 °C (Sm_2Co_7_550_H_2, $SmCo_5$_550_H_2).

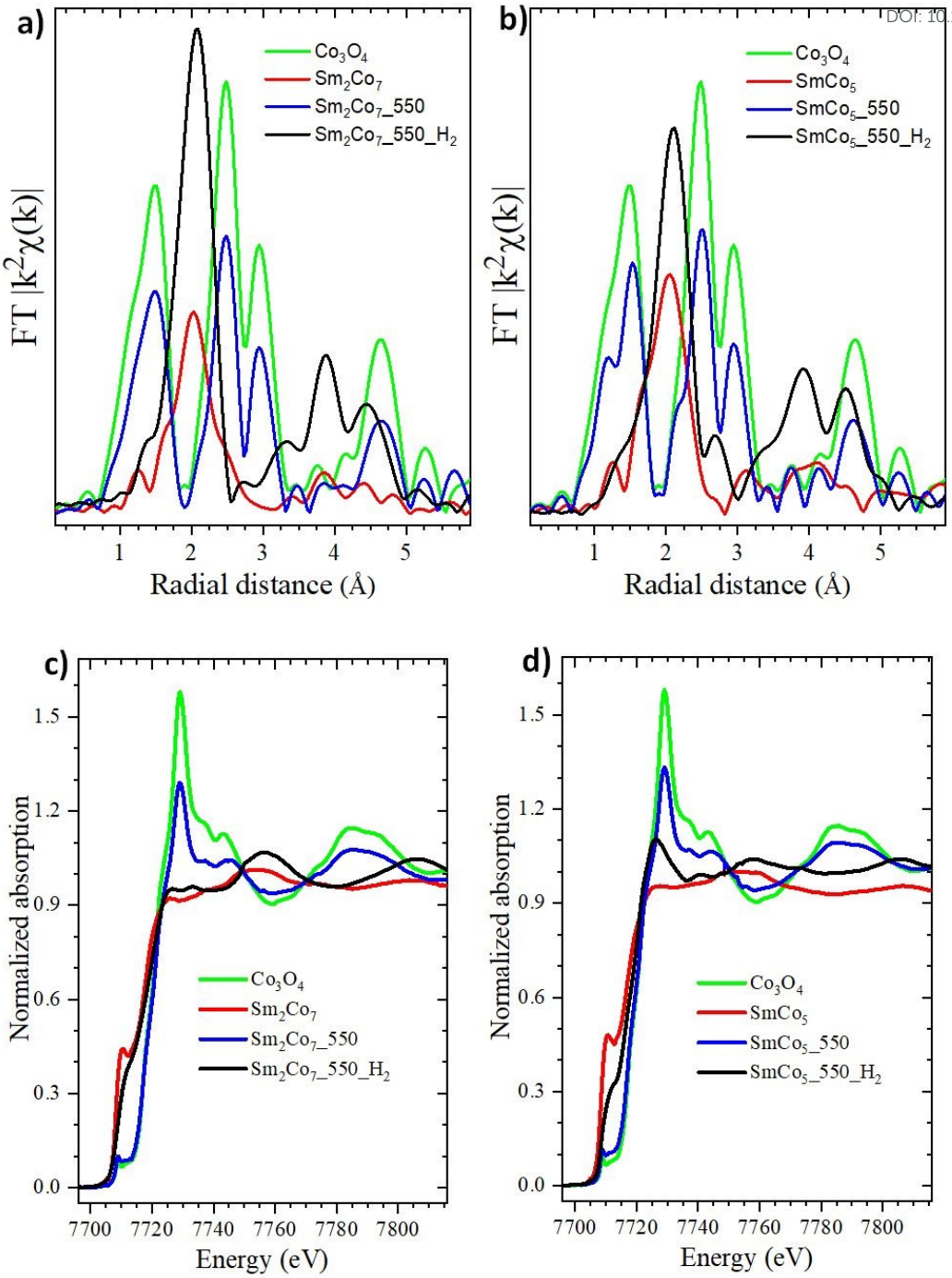

Figure 2. Fourier transform (FT) magnitude of Co K-edge EXAFS and Co K-edge XANES of Sm_2Co_7 (a&c) and $SmCo_5$(b&d) derived catalysts along with Co_3O_4.

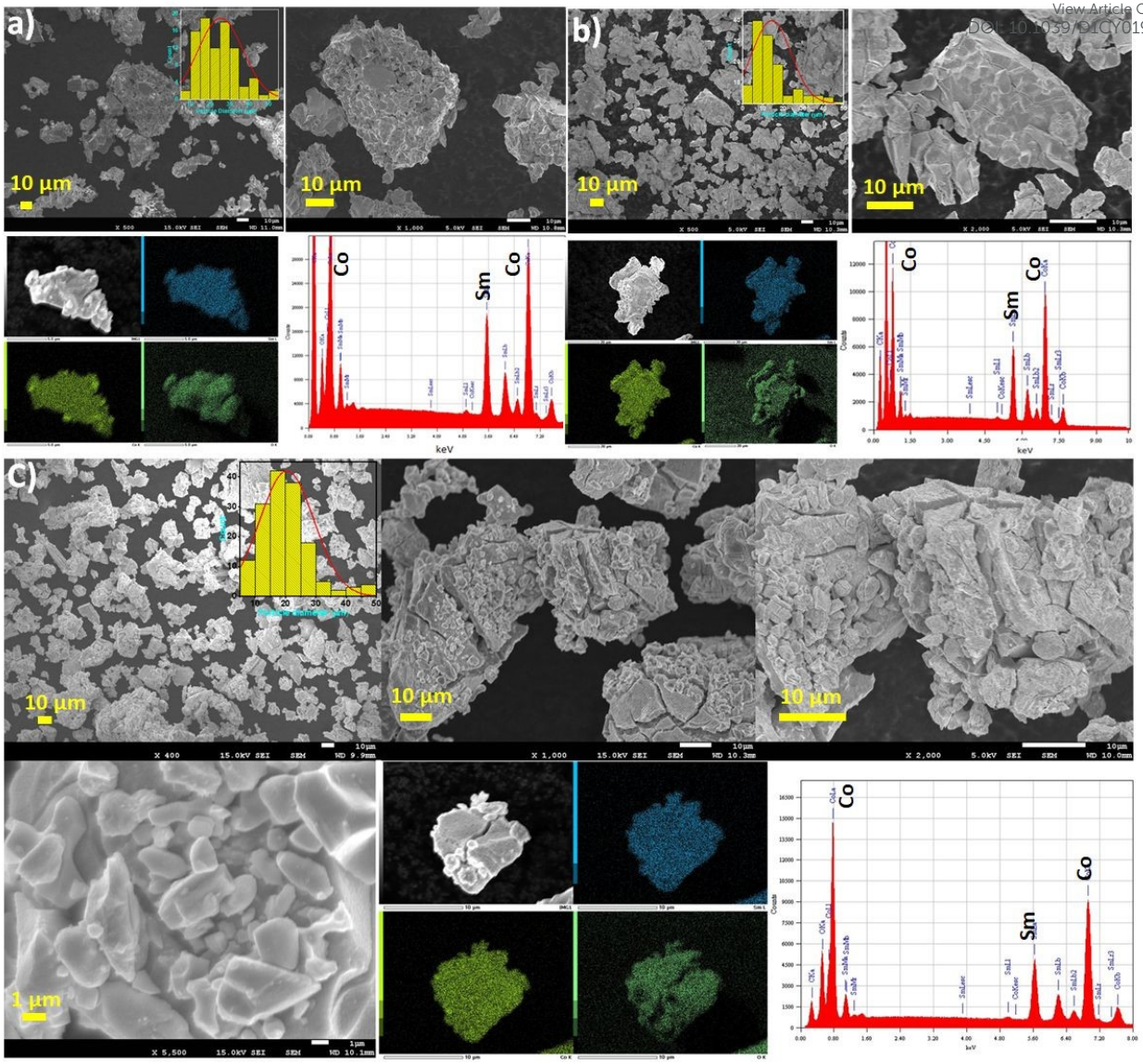

Figure 3. SEM images, particle size distribution, color mapping (Blue-Sm, Yellow, Co, Green -O) and EDAX spectra of a) Sm_2Co_7 b) Sm_2Co_7_550, and C) Sm_2Co_7_550_H_2.

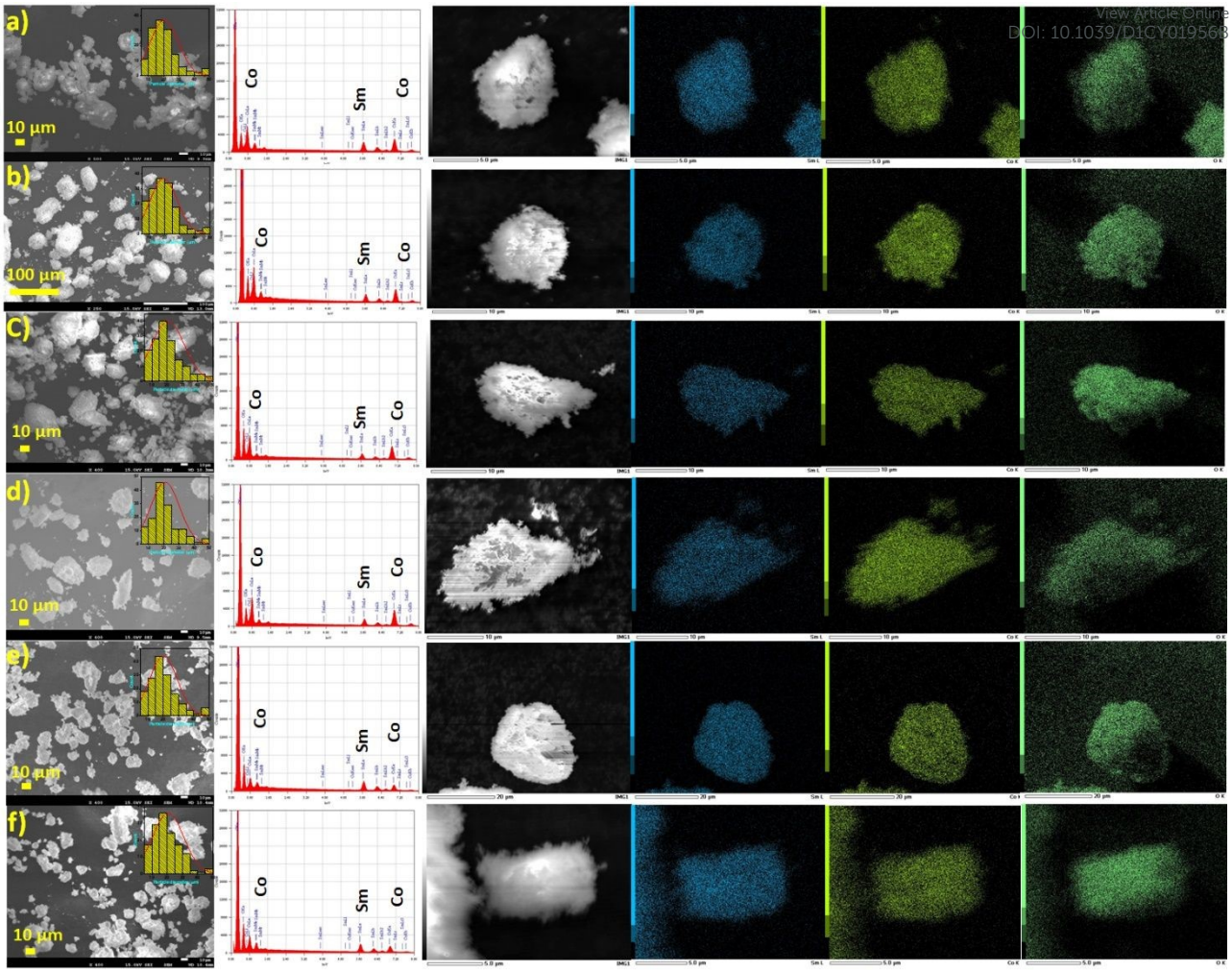

Figure 4. SEM images, particle size distribution, EDAX spectra and color mapping (Blue-Sm, Yellow-Co, Green -O) and of a) Sm_2Co_7_HT1 b) Sm_2Co_7_HT2, c) $SmCo_5$_HT1 d) $SmCo_5$_HT2 e) Sm_5Co_7_HT1 and f) Sm_5Co_7_HT2.

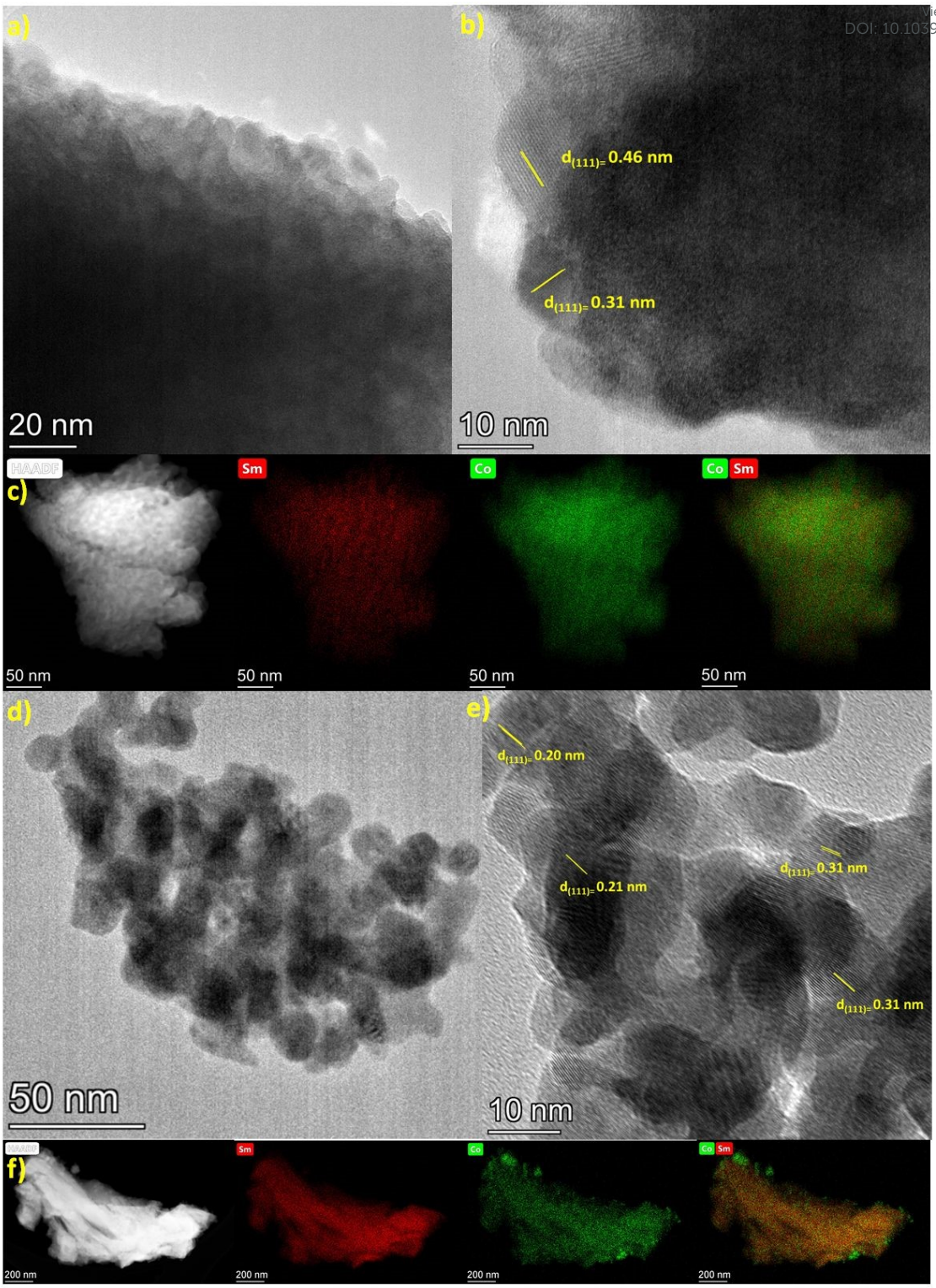

Figure 5. HAADF-STEM images and elemental colour mapping of Sm_2Co_7_550(a-c) and Sm_2Co_7_550_H_2(d-f).

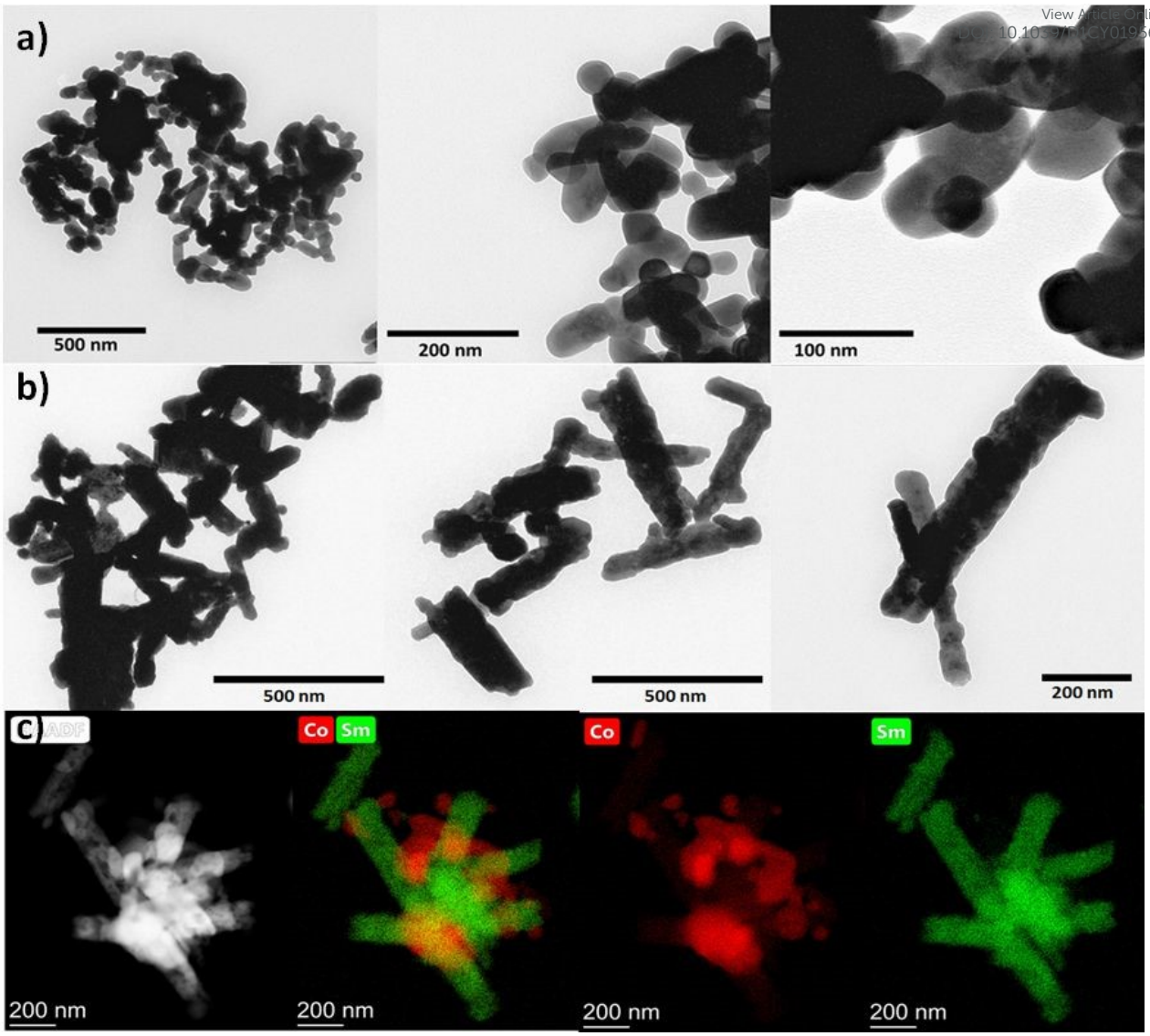

Figure 6. TEM images of a) Sm_2Co_7 HT1, b) Sm_2Co_7 HT2 and HAADF-STEM elemental colour mapping of Sm_2Co_7 HT2.

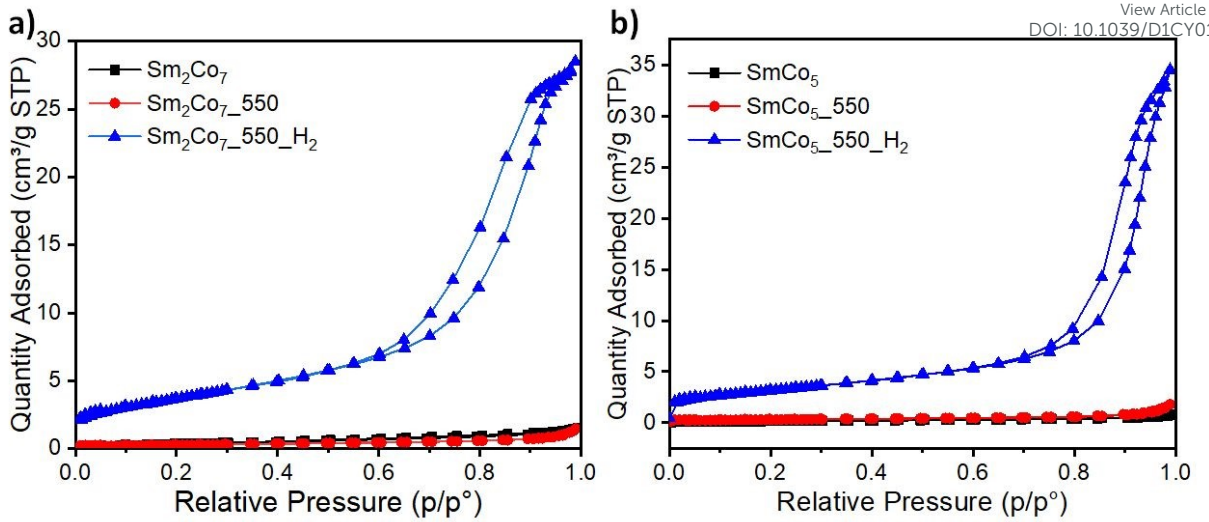

Figure 7. N_2 adsorption-desorption isotherm of a) Sm_2Co_7 and b) $SmCo_5$ IMC derived catalysts.

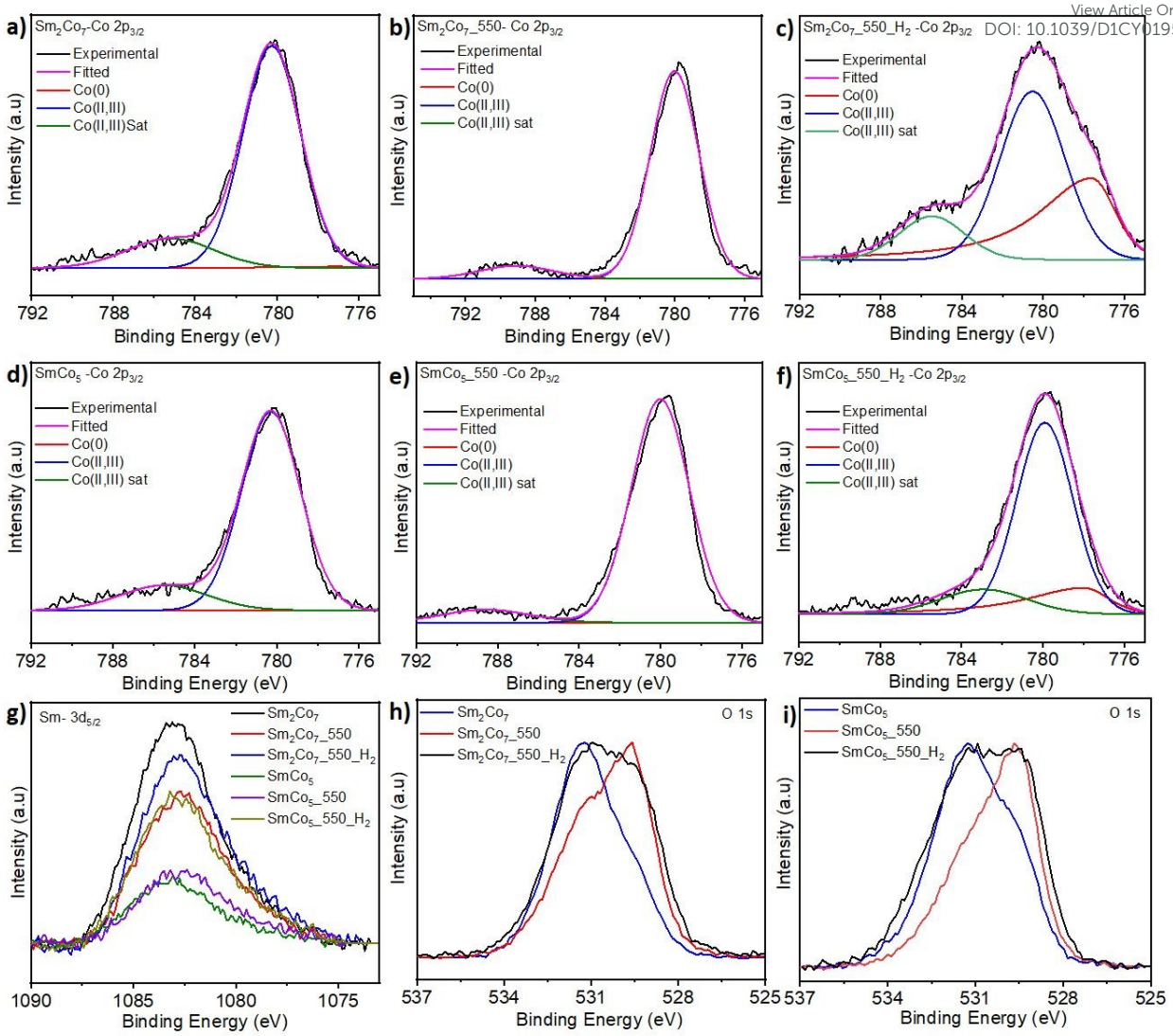

Figure 8. Co $2p_{3/2\ XPS}$ spectra of Sm_2Co_7, (a-c) and $SmCo_5$ IMC derived catalysts (d-f). Sm $3d_{5/2}$ XPS spectra of Sm_2Co_7 and $SmCo_5$ IMC derived catalysts(g). XPS spectra of O 1s (h-i).

View Article Online
DOI: 10.1039/D1CY01956B

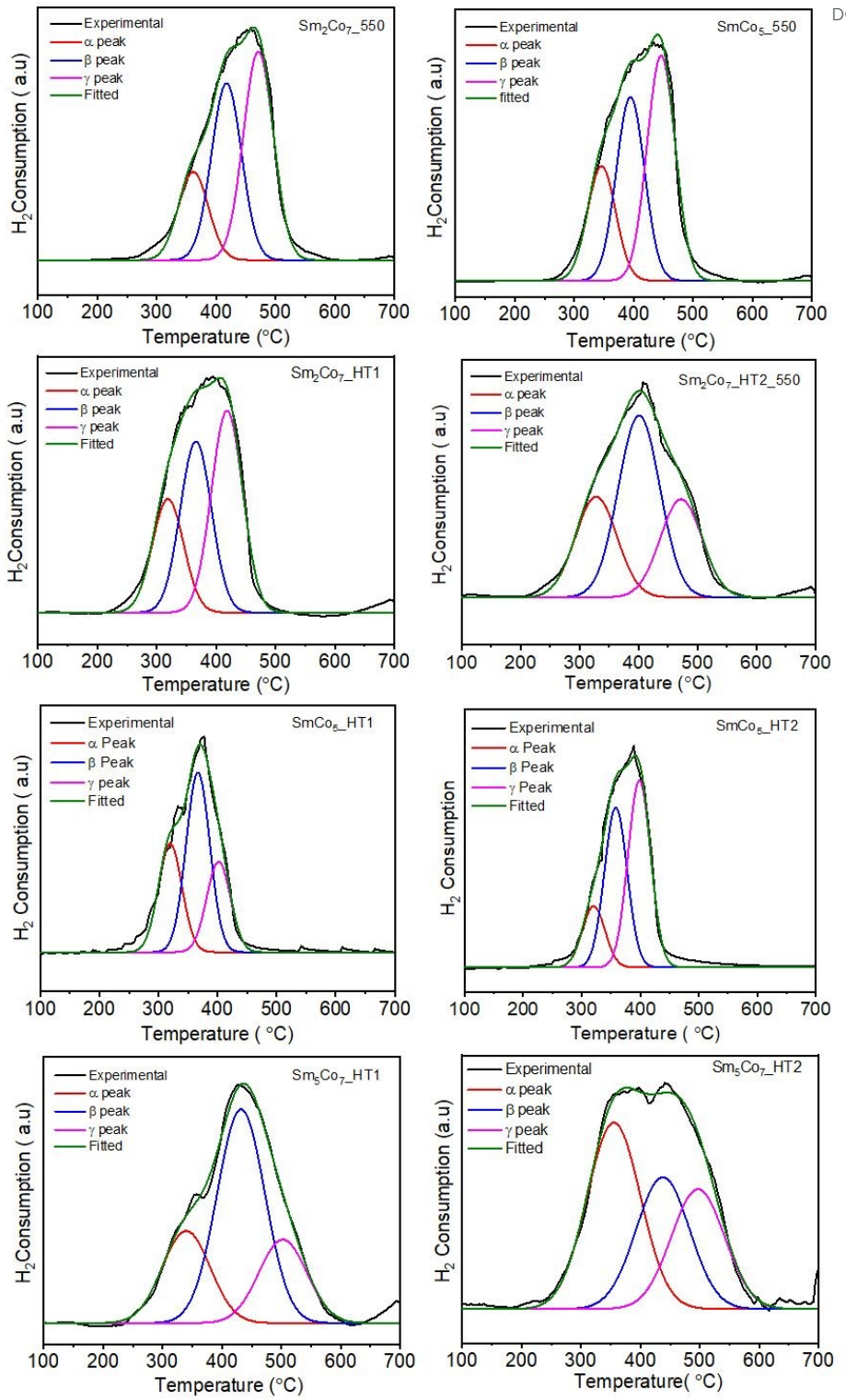

Figure 9. Deconvolution of TPR thermograms of the Sm_xCo_y catalysts.

View Article Online
DOI: 10.1039/D1CY01956B

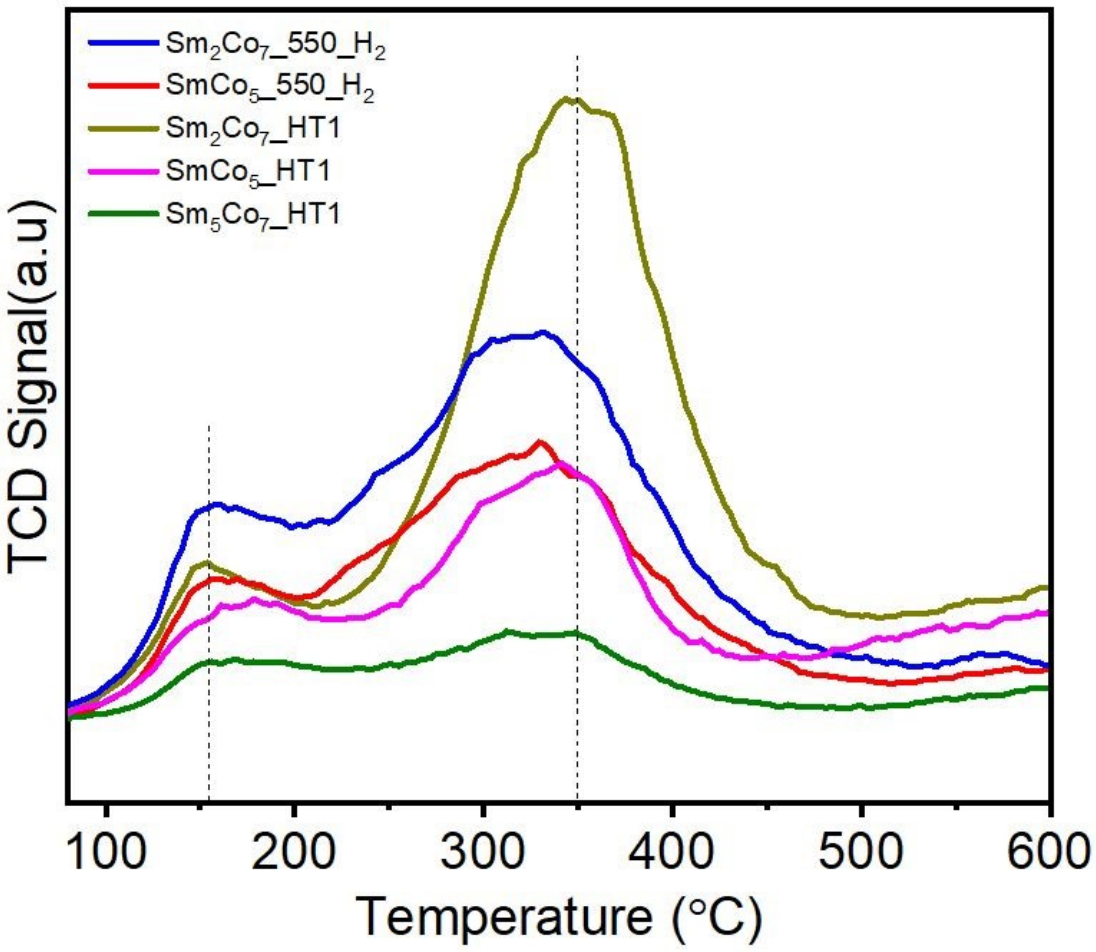

Figure 10. CO_2-temperature programmed desorption profiles of Co_Sm_2O_3 catalysts.

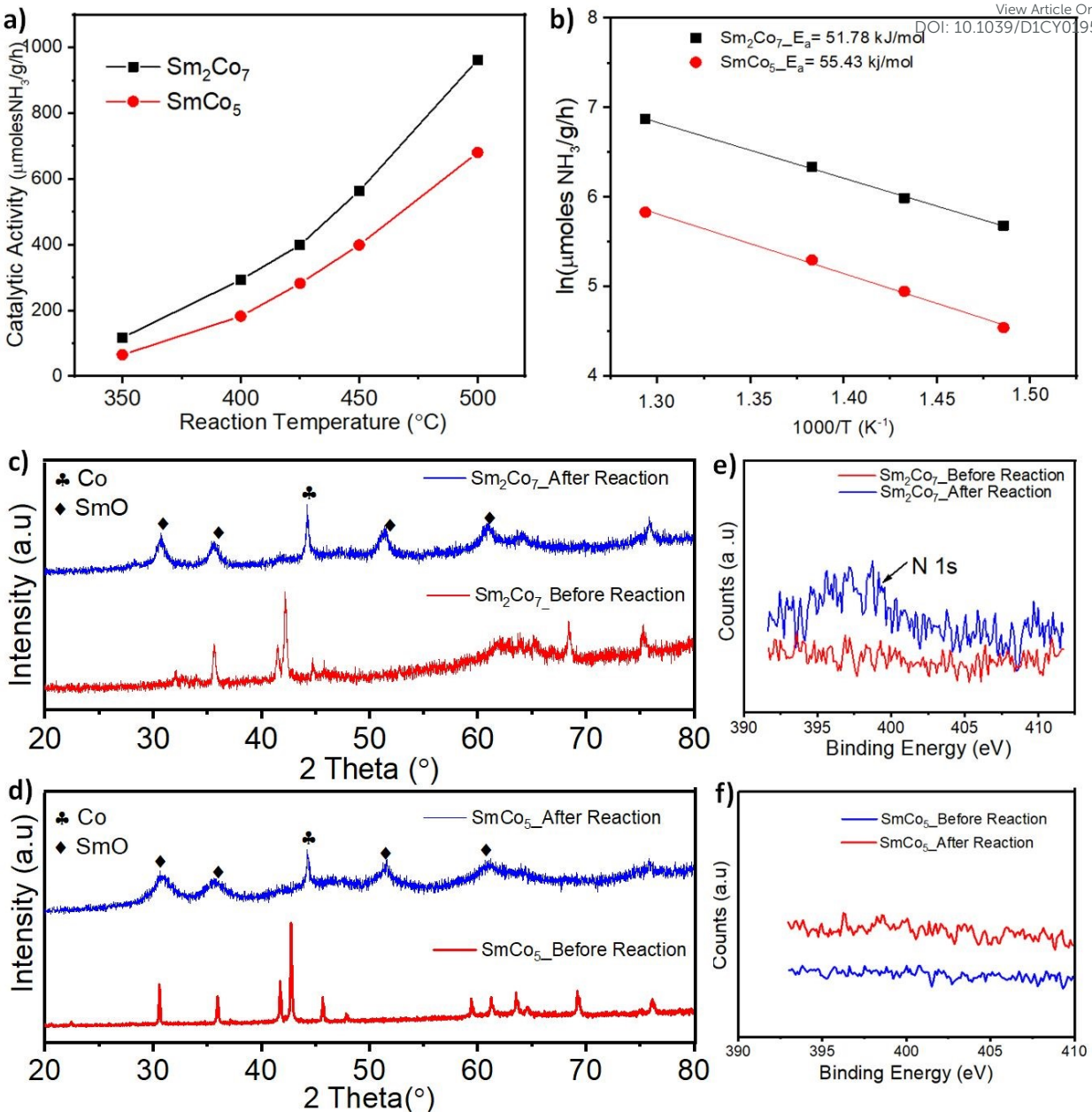

Figure 11. Ammonia synthesis rate(a) and activation energy profile (b) of pure Sm_2Co_7 and $SmCo_5$ compounds. (Reaction Conditions: H_2:N_2=3:1, Total Flow = 60ml/min, P=0.4 MPa, T= 500 °C, Catalyst = 0.2 g, XRD (c&d) and XPS N1s peak (e&f) of Sm_2Co_7 and $SmCo_5$ before and after reaction.

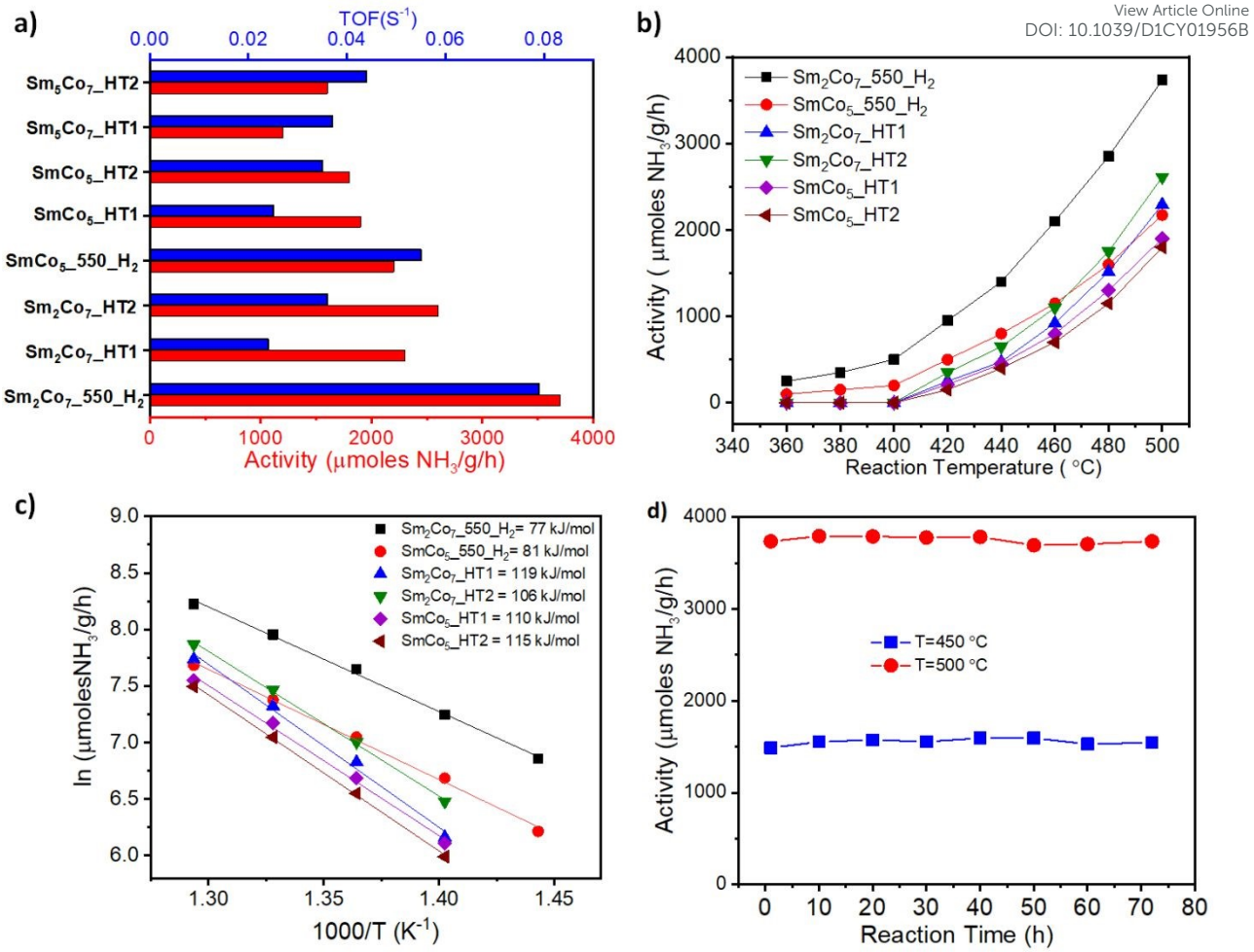

Figure 12. a) Activity and TOF of all the Co_Sm_2O_3 catalysts in NH_3 synthesis, b) Ammonia synthesis rate at different reaction temperatures, c) Arrhenius Plots of the catalysts, d) Time on stream study of Sm_2Co_7_550_H_2. (Rection Conditions : N_2= 15 ml/min, H_2= 45 ml/min, Catalyst =0.2 g, Pressure=0.4 MPa, T= 500 °C, 450 °C)

View Article Online
DOI: 10.1039/D1CY01956B

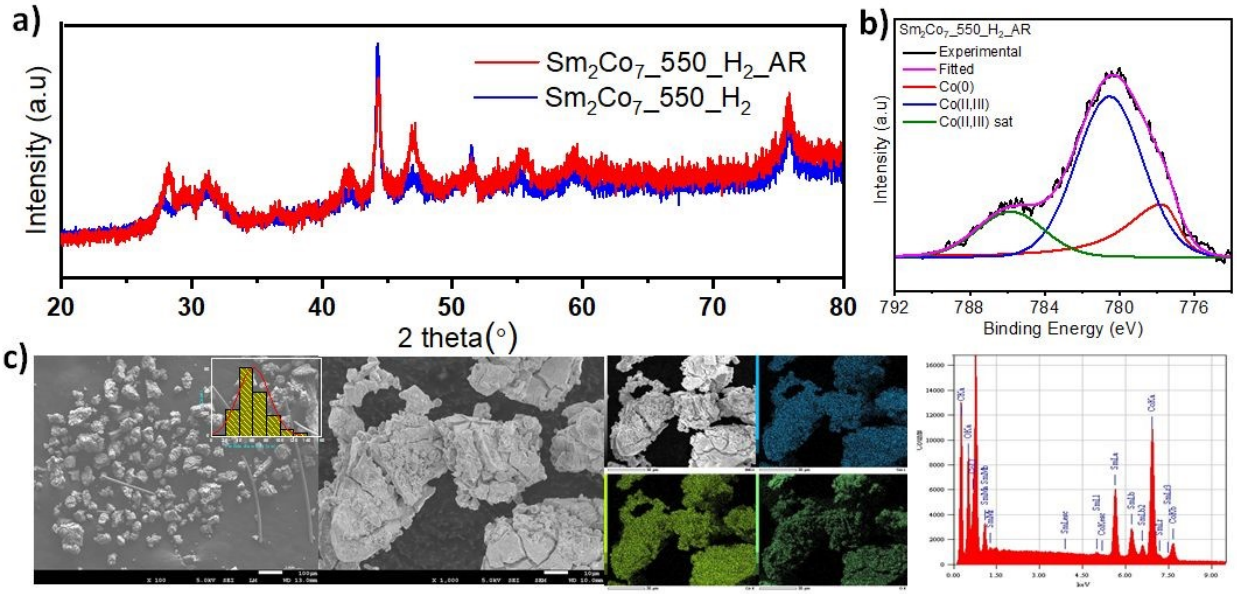

Figure 13. a) XRD patterns fresh and after reaction (AR) of Sm_2Co_7_550_H_2. b) Co $2p_{3/2}$ XPS spectra of recycled catalyst, and c) SEM images, particle size distribution, colour mapping and EDAX spectra of recycled catalyst.

View Article Online
DOI: 10.1039/D1CY01956B

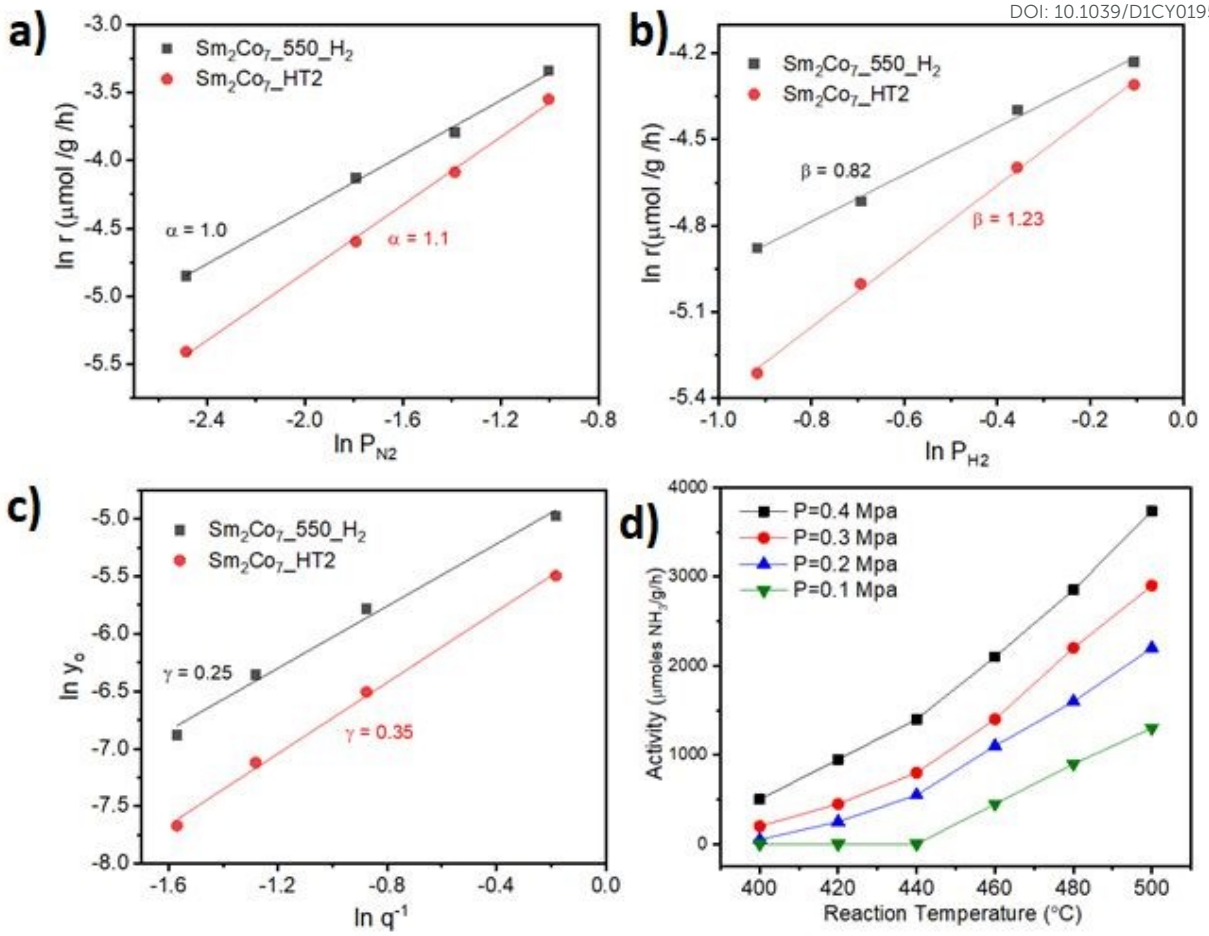

Figure 14. Dependency of reaction rate on the partial pressure of a) N_2, b) H_2, c) Dependence of ammonia partial pressures on the mixed gas flow rates. (slope = 1/(1-γ) and, d) Ammonia Synthesis rate at different temperatures as a function of total pressure.

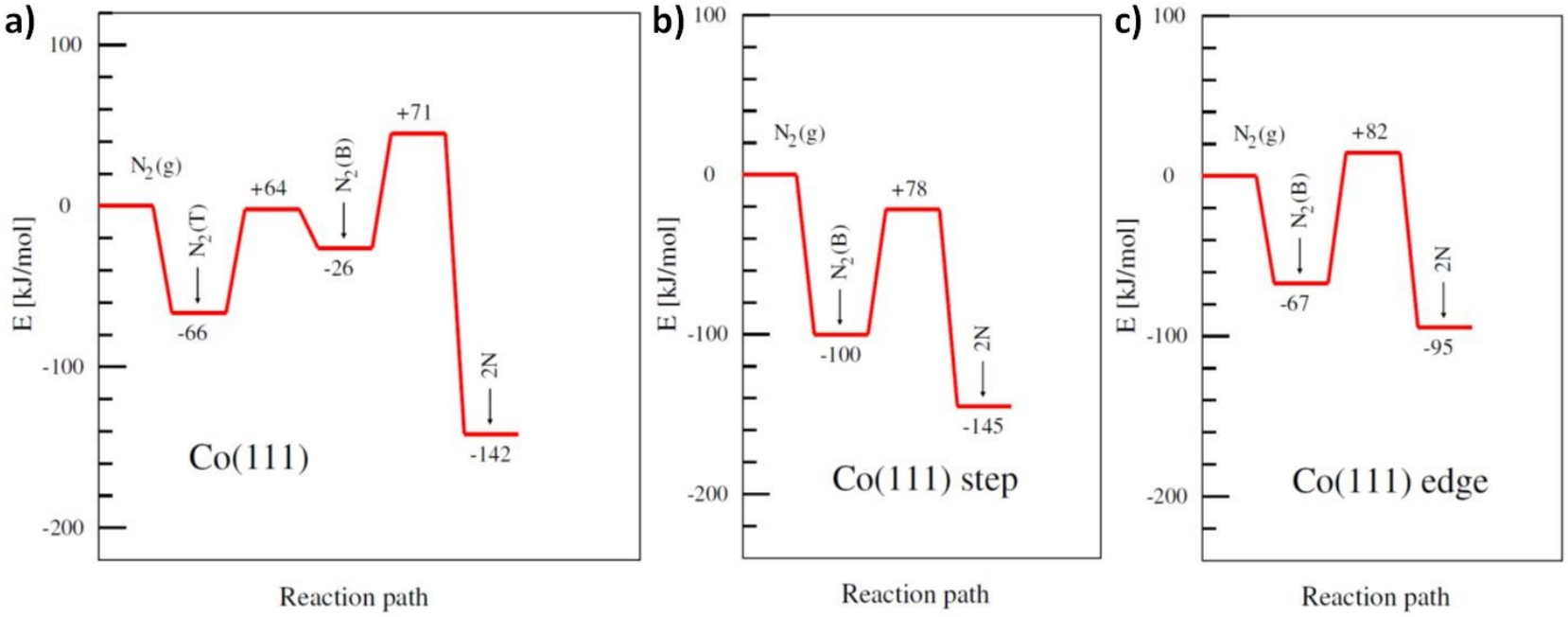

Figure 15. Energy profile of dissociation path of N2 adsorbed a) on the flat Co (111) surface, b) on as surface step and c) in the edge between two (111) surfaces

View Article Online
DOI: 10.1039/D1CY01956B

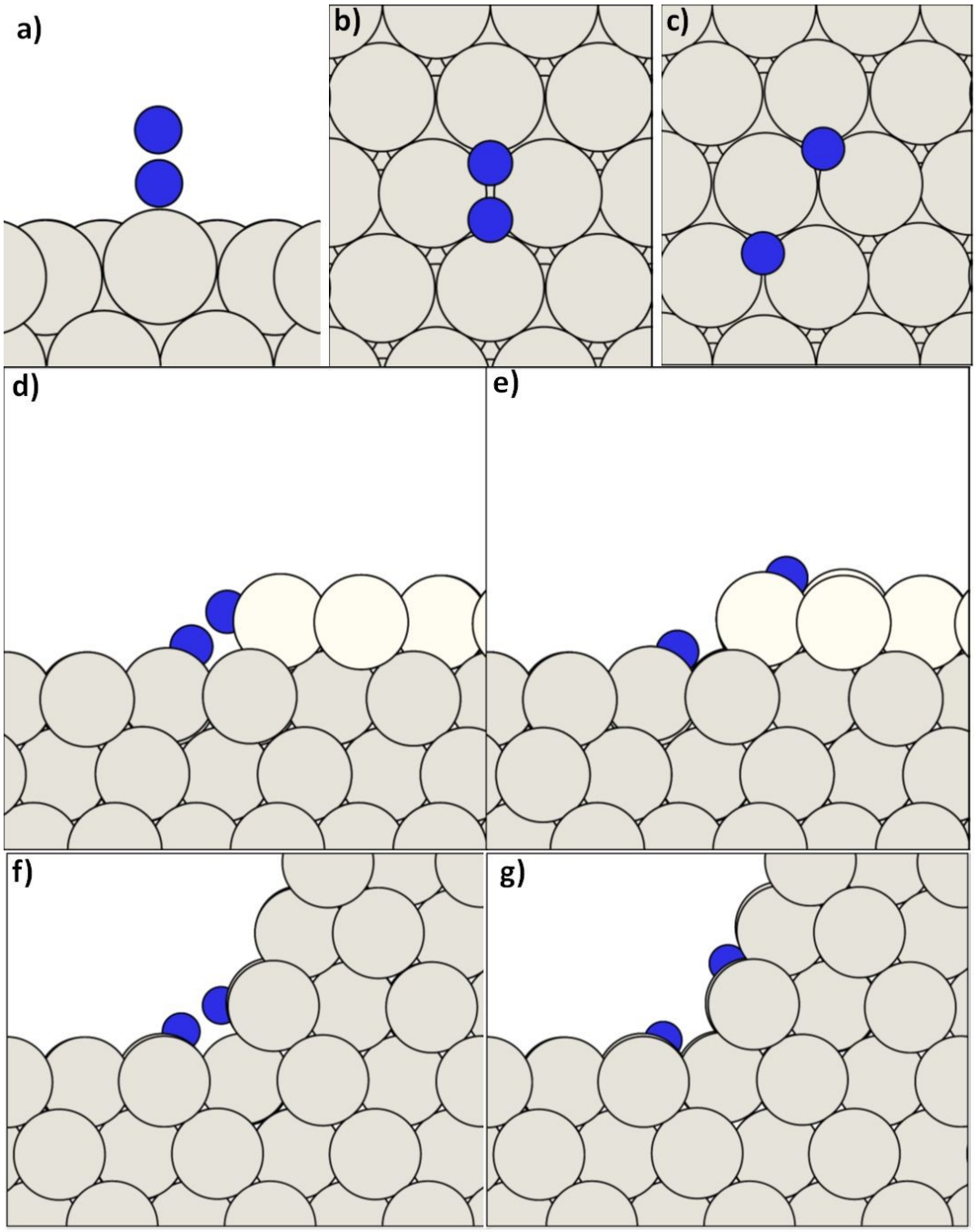

Figure 16. A view on N_2 adsorbed (a-c) on the flat, (d-e) surface step and (f-g) edge surfaces before and after dissociation.

View Article Online
DOI: 10.1039/D1CY01956B

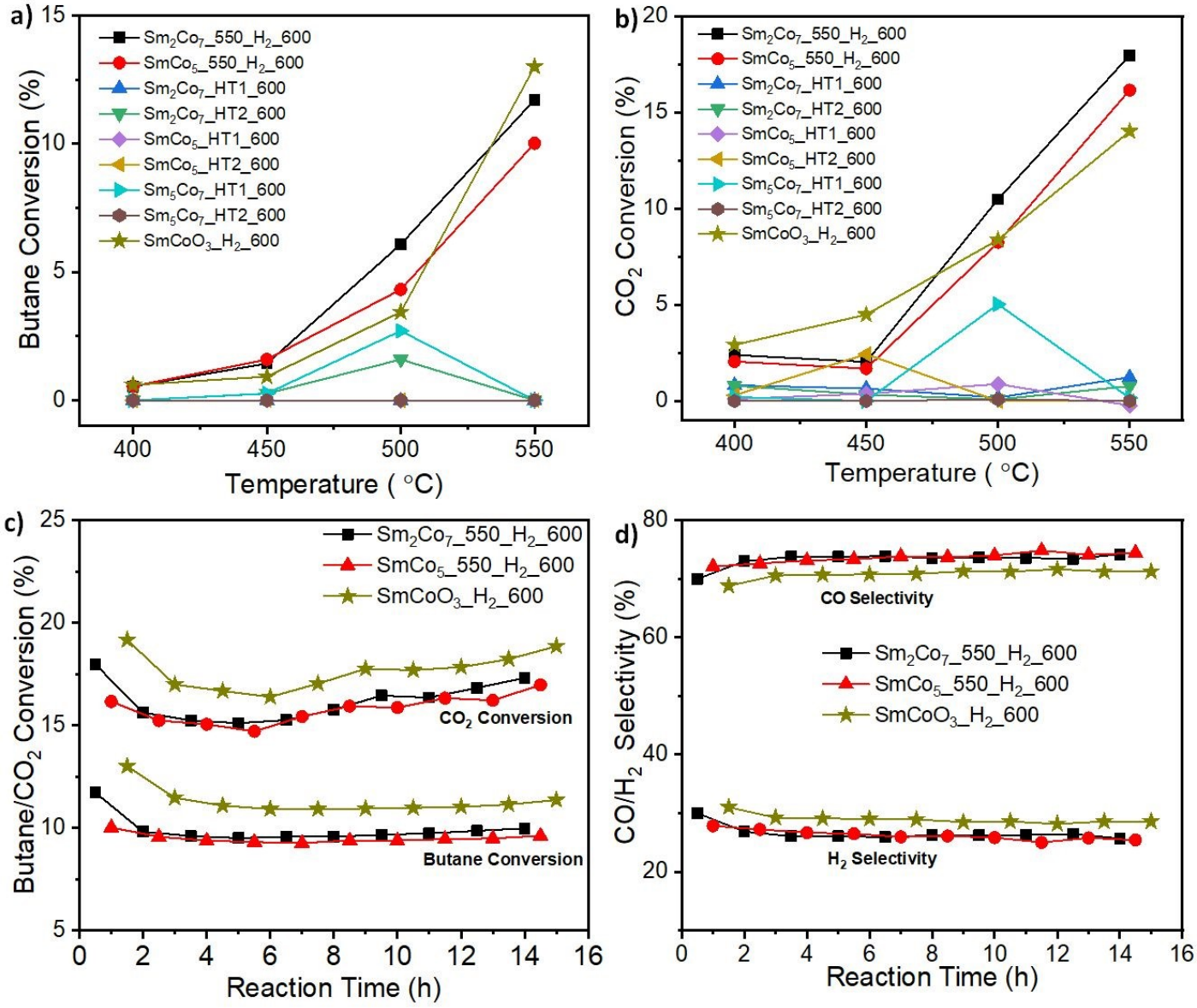

Figure 17. a) Butane and b) CO_2 conversions during the temperature screening tests of the Co_3O_4_Sm_2O_3 catalysts. (Reaction Conditions: 100 mg catalyst, CO_2/C_4H_{10} =4:1, Flow Rate =20 ml/min, atmospheric pressure) c) CO_2 and butane conversions along with d) CO and H_2 selectivity during the stability test. (Reaction conditions: 100 mg catalyst, CO_2/C_4H_{10} =4:1, Flow Rate =20 ml/min, Temp= 550 °C)

Table 1. Physiochemical properties of Sm_xCo_y catalysts and their catalytic activity in NH_3 synthesis.

Catalysts	Co/Sm (EDAX)	Co/Sm (XPS)	Surface Area (m^2/g)	CO chemisorption (µmoles/g)	Basicity (µmoles/g)	Co/Sm (Co-Chemisorption /TPD-CO_2)	NH_3 synthesis rate (µmol/g/h)	TOF (sec^{-1}) ^{CO}
Sm_2Co_7	3.5	2.4	1	-	-	-	0950	--
Sm_2Co_7_550_H_2	3.5	2.2	13	13	78	0.14	3700	0.079
Sm_2Co_7_HT1	3.0	2.7	19	26	98	0.26	2300	0.024
Sm_2Co_7_HT2	3.5	1.1	12	20	72	0.27	2600	0.036
$SmCo_5$	5.0	2.1	1	-	-	-	0700	--
$SmCo_5$_550_H2	5.0	2.5	11	11	63	0.20	2200	0.055
$SmCo_5$_HT1	4.5	2.1	10	21	57	0.36	1900	0.025
$SmCo_5$_HT2	5.0	1.5	07	14	45	0.31	1800	0.035
Sm_5Co_7_HT1	1.3	0.4	06	09	31	0.22	1200	0.037
Sm_5Co_7_HT2	1.4	1.1	06	10	52	0.19	1600	0.044
$SmCoO_3$_500	1.0	1.0	05	08	25	0.28	1000	0.035

Reaction Conditions: H_2:N_2=3:1, Total Flow = 60ml/min, P=0.4 MPa, T= 500 °C, Catalyst = 0.2 g.

View Article Online
DOI: 10.1039/D1CY01956B

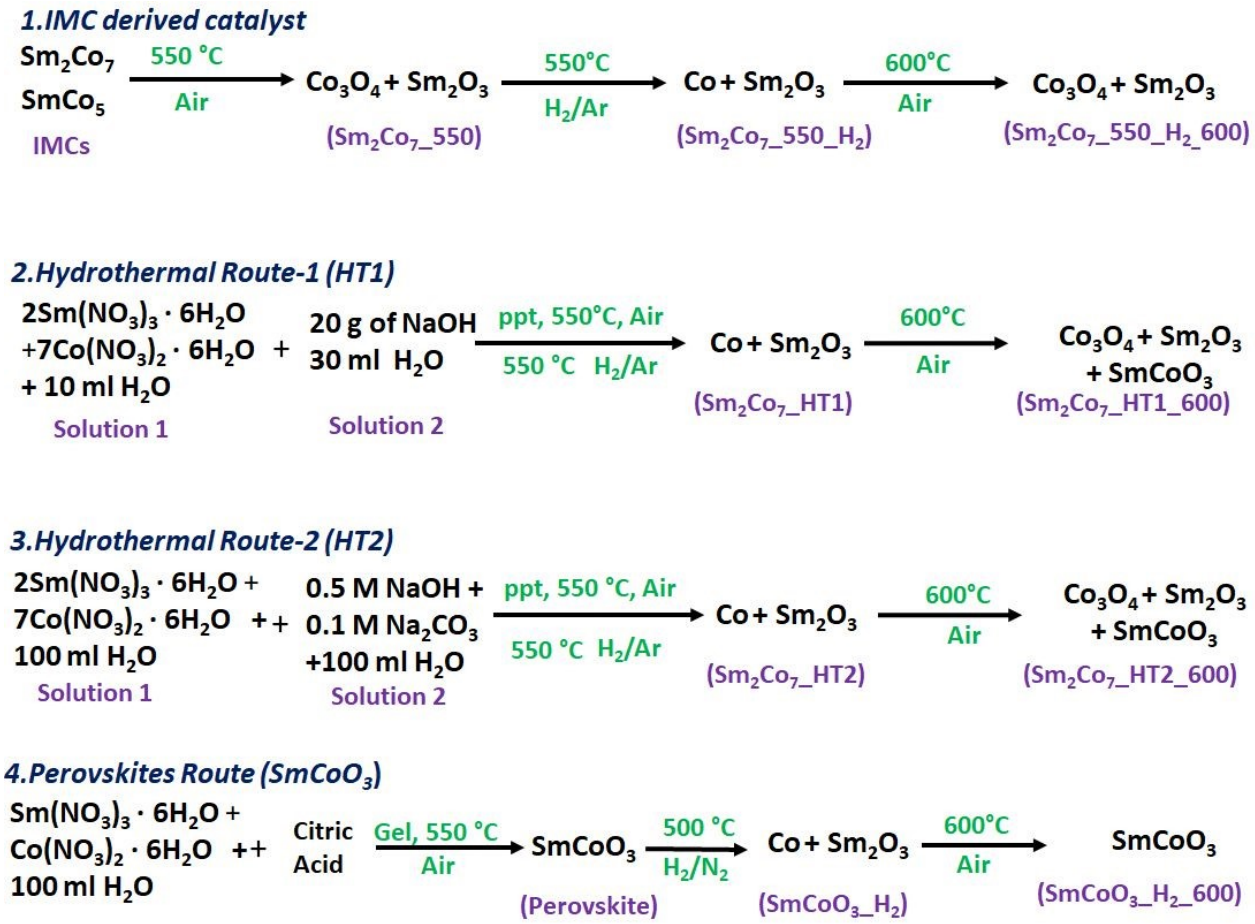

Scheme 1. Schematic representation for the synthesis Co_Sm_2O_3 and Co_3O_4_Sm_2O_3 by 1) Intermetallic Compounds, 2&3) Hydrothermal method 4) Perovskite route.

View Article Online
DOI: 10.1039/D1CY01956B

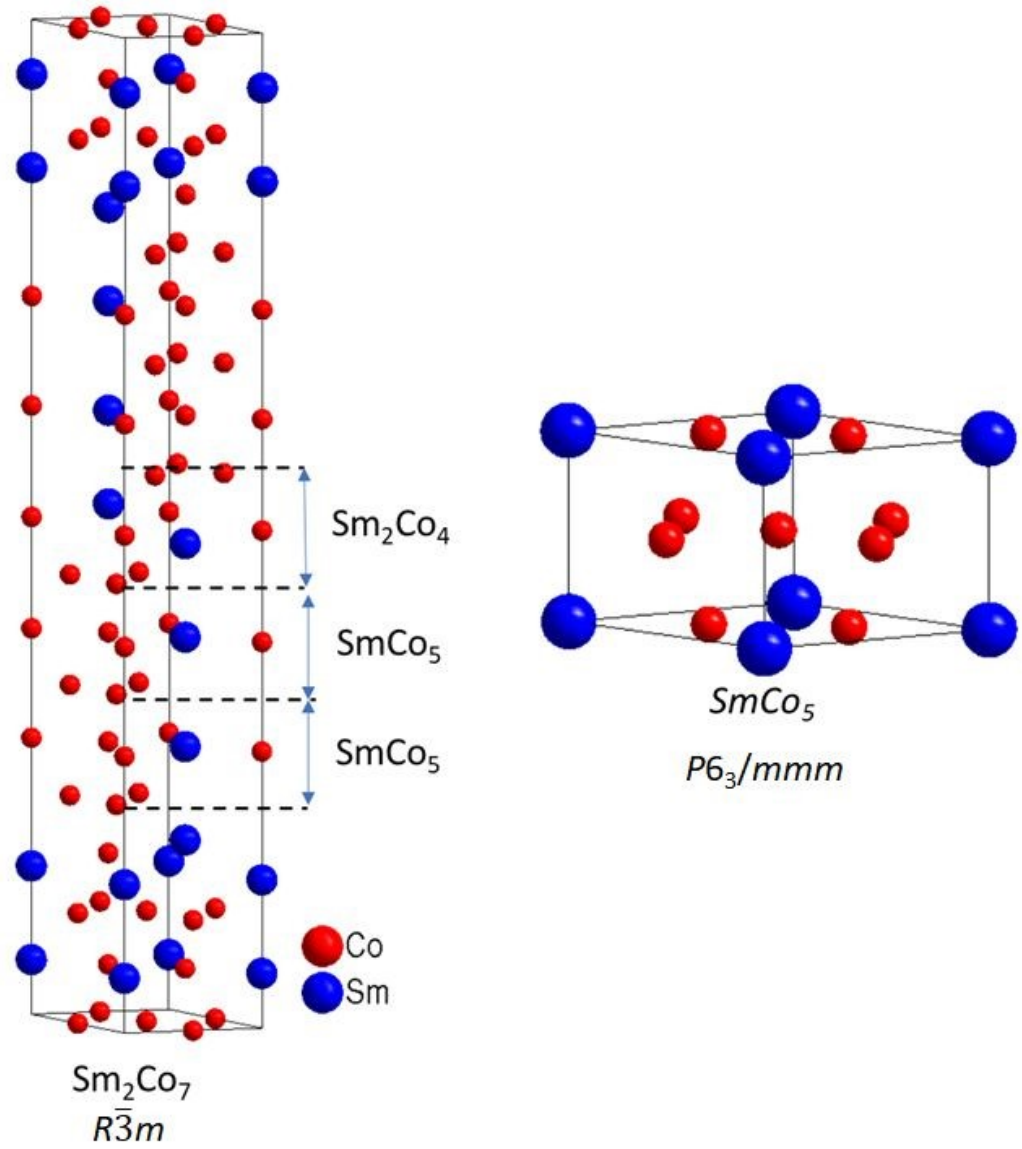

Scheme 2. Crystal structure of rhombohedral Sm_2Co_7 and hexagonal $SmCo_5$ Intermetallic compounds.